



On-line adaptive battery impedance parameter and state estimation considering physical principles in reduced order equivalent circuit battery models:



Part 2. Parameter and state estimation

Christian Fleischer^{a,c,*}, Wladislaw Waag^{a,c}, Hans-Martin Heyn^{a,c}, Dirk Uwe Sauer^{a,b,c}

^aElectrochemical Energy Conversion and Storage Systems Group, Institute for Power Electronics and Electrical Drives (ISEA), RWTH Aachen University, Jägerstrasse 17/19, 52066 Aachen, Germany

^bInstitute for Power Generation and Storage Systems (PGS), E.ON ERC, RWTH Aachen University, Germany

^cJülich Aachen Research Alliance, JARA-Energy, Germany

HIGHLIGHTS

- Algorithm for estimating battery impedance parameters and states (SoC, SoH, SoF).
- Represented as a nonlinear equivalent circuit model with temperature dependency.
- Current dependency of battery impedance is considered by parameter estimation.
- Universally applicable to all battery technologies without the need of cell testing.
- Real-time capability for implementation on low-cost microcontroller.

ARTICLE INFO

Article history:

Received 8 January 2014
Received in revised form
16 February 2014
Accepted 13 March 2014
Available online 27 March 2014

Keywords:

Battery monitoring
Parameter & state estimation
Impedance
On-line recursive algorithm

ABSTRACT

Lithium-ion battery systems employed in high power demanding systems such as electric vehicles require a sophisticated monitoring system to ensure safe and reliable operation. Three major states of the battery are of special interest and need to be constantly monitored. These include: battery state of charge (SoC), battery state of health (capacity fade determination, SoH), and state of function (power fade determination, SoF). The second paper concludes the series by presenting a multi-stage online parameter identification technique based on a weighted recursive least quadratic squares parameter estimator to determine the parameters of the proposed battery model from the first paper during operation. A novel mutation based algorithm is developed to determine the nonlinear current dependency of the charge-transfer resistance. The influence of diffusion is determined by an on-line identification technique and verified on several batteries at different operation conditions. This method guarantees a short response time and, together with its fully recursive structure, assures a long-term stable monitoring of the battery parameters. The relative dynamic voltage prediction error of the algorithm is reduced to 2%. The changes of parameters are used to determine the states of the battery. The algorithm is real-time capable and can be implemented on embedded systems.

© 2014 Elsevier B.V. All rights reserved.

1. Introduction

This is the second paper in a series that describes advanced algorithms for battery monitoring for electric and hybrid electric vehicles (EVs, HEVs). Battery management systems (BMS) for large

lithium-ion battery packs, as they can be found in electric vehicles, take on a variety of tasks. The BMS must receive measurements, analyze and evaluate the incoming data, perform management operations according to the analyzed data, communicate with surrounding and depending systems such as the drive train of the vehicle, and log all events for potential fault analysis. Besides the measurement hardware for data acquisition with standard functions, the real key function of the BMS are the corresponding monitoring algorithms, that provide the necessary information about the battery parameter and states, e.g. state of charge (SoC),

* Corresponding author. Electrochemical Energy Conversion and Storage Systems Group, Institute for Power Electronics and Electrical Drives (ISEA), RWTH Aachen University, Jägerstrasse 17/19, 52066 Aachen, Germany. Tel.: +49 241 80 97158; fax: +49 241 80 92203.

E-mail address: cfl@isea.rwth-aachen.de (C. Fleischer).

state of health (SoH), available charging and discharging power, capacity, battery impedance parameters and residual energy. Thereby, it is of particular interest to identify the change of described states initiated by battery aging. The algorithms developed to estimate the battery impedance parameters are based on a recursive weighted least quadratic square estimator. This estimator is faster in convergence and simpler in comparison to Kalman filtering in terms of required knowledge of noise statistics and computational cost. The first paper was an introduction to the challenges of BMS by giving a critical review including a large number of scientific papers and patents regarding this topic. On that basis, the requirements on intelligent and memory optimized monitoring algorithms are analyzed. This leads to a step-by-step implementation of the mathematical cell model, which includes the influence of the Butler–Volmer kinetics on the charge-transfer process. Furthermore, the mass transport process inside the battery is modeled in a novel state-space representation.

The second paper covers the real-time parameter and state estimation problem; such as on-line estimation of battery impedance parameter for SoC, SoH, and available power and so forth. The parameters of the battery model derived in the first paper are adaptable and tracked in order to identify battery aging effects. Therefore, a method for identifying on-line battery impedance parameters using a weighted recursive least quadratic square parameter estimator is presented. A state of charge determination algorithm is derived based on the residual term of the least-square parameter identification algorithm. Because the parameters of the battery model are updated online, the state of health can be tracked by observing the change of battery impedance parameters. Especially the increase of the charge-transfer resistance reflects the aging process. To evaluate the state of function, the charging and discharging power capability of the battery is analyzed by evaluating the identified resistances of the battery model. The identified parameters and states are verified on several batteries and at different operation and aging conditions (Table 1).

2. Weighted recursive least quadratic square parameter estimator

In this section a parameter estimator based on a weighted least quadratic square method is employed. The estimator approach is formulated in a recursive manner to allow the implementation into a digital control system.

In our first paper piecewise linear regression model is derived to describe the main nonlinear battery dynamics in the equivalent circuit model.

$$\hat{y}(k, \theta_d(k)) = \varphi^T(k) \theta_d(k) \quad (1)$$

The vector $\varphi(k)$ contains the regressors in Eq. (2)

$$\varphi(k) = \begin{pmatrix} u(k) \\ u(k-1) \\ y(k) \\ 1 \end{pmatrix} \quad (2)$$

and the vector $\theta_d(k)$ describes the parameters in Eq. (3)

$$\theta_d = \begin{pmatrix} b_0 \\ b_1 \\ a_1 \\ e \end{pmatrix} \quad (3)$$

that are to be estimated. The aim is to determine the parameter vector θ_d for a moment in time k so that the predicted voltage $\hat{y}(k, \theta_d(k))$ is as close as possible to the measured voltage $y(k)$. The error between the predicted and the actual voltage can be written as

$$\varepsilon(k, \theta_d(k)) = y(k) - \varphi^T(k) \theta_d(k) \quad (4)$$

which is known as the prediction error given by our model $\mathcal{M}(\theta_d(k))$ [1].

According to Ljung et al. in Ref. [1] a quadratic norm can be used as suitable norm to describe the development of the error for a given set of data Z^N with a given number N of samples $k = 1, 2, 3, \dots, N$.

$$C_N(\theta_d, Z^N) = \frac{1}{N} \sum_{k=1}^N 0.5 \cdot (y(k) - \varphi^T(k) \theta_d(k))^2 \quad (5)$$

The norm Eq. (5) is known as least-quadratic-square criterion function of the regression Eq. (1) or simply cost function of the problem. The optimal set of parameters θ_d is obtained when the cost function reaches its minimum.

$$\hat{\theta}_d(k) = \arg \min_{\theta_d} C_N(\theta_d, Z^N) \quad (6)$$

Since Eq. (6) is a quadratic function in θ_d its minimization forms a convex optimization problems which can be solved analytically [1]. Thus the aim of finding an optimal set of parameters θ_d is reduced to solving the least-square estimate function Eq. (7) [1].

$$\hat{\theta}_d(k) = \left(\frac{1}{N} \sum_{k=1}^N \varphi(k) \varphi^T(k) \right)^{-1} \cdot \frac{1}{N} \sum_{k=1}^N \varphi(k) y(k) \quad (7)$$

2.1. Influence of past data samples on parameter estimate

Ideally the regression term Eq. (1) describes a linear system. This is not the case for the equivalent circuit model of a battery which behaves strongly nonlinear. However it can be assumed that around a certain working point the battery acts in a linear way and can be described by a piecewise linear system [2]. The parameter

Table 1
An overview of cells used for parameter estimation validation.

Cell name	Manufacturer	Type	Nominal cap.	Present cap.	Initial cap.	Aging state	Technical specification	
							Max. charging current/voltage	Max. discharging current/voltage
Cell K-1	Kokam	SLPB100216216H	40 Ah	42.5 Ah	42.5 Ah	New cell	120 A/4.2 V	320 A/3.0 V
Cell K-2				38 Ah	42.4 Ah	Significantly aged		
Cell S-1	Sanyo	UR18650E	2.05 Ah	2.01 Ah	2.01 Ah	New cell	2.05 A/4.2 V	15 A/2.5 V
Cell S-2				1.82 Ah	2.05 Ah	Aged cell		
Cell O-1	OMT	OMLIFE8AHC-HP	8 Ah	8.2 Ah	8.2 Ah	New cell	80 A/3.65 V	240 A/3.2 V
Cell O-2				7.1 Ah	8.2 Ah	Aged cell		

set for the equivalent circuit model depends, as mentioned before, on the temperature and the state of charge which both might change during operation of the battery cell [3]. The more measurements for current $u(k - n)$ and voltage $y(k - n)$ and thus the value of the regression-vector $\phi(k - n)$ are in the past, the less accurate the estimates they produce for the parameter-vector $\theta_d(k)$ are. The reason is that the working point of the battery has changed in the meantime and thus the parameters in θ_d will have changed, too. Therefore a temporal weighting $\beta(N, k)$ is introduced to give the latest data more influence on the parameter estimate θ_d and slowly 'forget' older data. This results in a slightly modified version of the cost function Eq. (5) which incorporates the temporal weighting.

$$C_N(\theta_d, Z^N) = \sum_{k=1}^N \beta(N, k) \cdot (y(k) - \phi^T(k)\theta_d(k))^2 \quad (8)$$

The new cost function Eq. (8) leads to a modified optimization problem with a temporal weighting term $\beta(N, k)$.

$$\hat{\theta}_d(k) = \arg \min \sum_{k=1}^N \beta(N, k) \cdot (y(k) - \phi^T(k)\theta_d(k))^2 \quad (9)$$

The new optimization problem can again be solved analytically since it represents a convex optimization problem.

$$\hat{\theta}_d(k) = \left(\sum_{k=1}^N \beta(N, k) \cdot \phi(k)\phi^T(k) \right)^{-1} \cdot \sum_{k=1}^N \beta(N, k) \cdot \phi(k)y(k) \quad (10)$$

The temporal weighting term $\beta(N, k)$ contains a weighting sequence which is updated at each time step. This results in a memory with exponentially fading of past values of the input current $u(k)$ and output voltage $y(k)$. This ensures that the latest data sample has full influence on the new estimate of the parameter vector $\theta_d(k)$ and that past data samples exponentially lose influence on the estimate of the current parameter vector.

$$\beta(N, k) = \begin{cases} \lambda(k)\beta(N, k-1) & 0 \leq n \leq k-1 \\ 1 & n = k \end{cases} \quad (11)$$

The time until a data-sample Z^n collected at the discrete time step n has less than 1% influence depending on the forgetting factor λ can be calculated as follows.

$$T_\lambda = \frac{\ln 0.01}{\ln \lambda} \quad (12)$$

The temporal weighting $\beta(N, k)$ solely depends on the previous value of the temporal weighting $\beta(N, k-1)$ and the weighting factor λ . Thus Eq. (11) represents a recursive formulation for the temporal weighting term. This shall lead to the approach of reformulating the entire optimization problem Eq. (9) into a recursive form.

3. Recursive reformulation of the optimization problem

In order to allow the algorithm to work online the calculation of the optimal parameter set $\theta_d(k)$ must be done within one time step T_s . Furthermore to get access to the time continuous parameters the parameter vector $\theta_d(k)$ must be transformed to the continuous time parameter vector $\hat{\theta}(t)$ using Eq. (13) derived in our first paper.

$$\begin{aligned} b_0 &= R_i & R_i &= b_0 \\ b_1 &= \frac{T_s}{C} + \frac{T_s R_i}{C_{dl} R_{ct}} - R_i & R_{ct} &= \frac{b_1 - b_0 a_1}{a_1 + 1} \\ a_1 &= \frac{T_s}{C_{dl} R_{ct}} + 1 & C_{dl} &= \frac{T_s}{b_1 - b_0 a_1} \end{aligned} \quad (13)$$

That way the user can interpret the parameter for the continuous time equivalent circuit model. This might work for the first few samples of data. Even with a fading memory as described in Eq. (11) a huge amount of calculations must be conducted to solve the optimization problem Eq. (10). For example a sampling rate of $T_s = 0.1$ s is employed and the current time of the simulation is $T_n = 30$ min, which is a reasonable amount of time for a driving cycle within a city. That means that $N = 18,000$ samples will have been collected until this point, resulting in several ten thousand processing steps to find the optimal parameter vector. Even on modern computers it is not feasible to solve this optimization problem within one time step of $T_s = 0.1$ s. The size of the problem must be reduced in such a way that the processing time of one time step is sufficient to find the optimal parameter vector $\hat{\theta}_d(k)$.

Currently the set of optimal parameters from the previous time step $\hat{\theta}_d(k-1)$ is not considered in the calculation of the current optimal set of parameters $\hat{\theta}_d(k)$. If the result of this processing is stored in a memory for the next time step it can be used for the processing of a new set of optimal parameters $\hat{\theta}_d(k)$. According to Ljung in Ref. [1] the solution Eq. (10) for the optimal parameter set can be reformulated by introducing an auto-correlation term $R(k)$ and a correlation term $S(k)$.

$$\hat{\theta}_d(k) = R(k)^{-1} \cdot S(k) \quad (14)$$

$$R(n) = \sum_{k=1}^n \beta(n, k) \cdot \phi(k)\phi^T(k) \quad (15)$$

$$S(n) = \sum_{k=1}^n \beta(n, k) \cdot \phi(k)y(k)$$

With the help of the definition of the fading memory Eq. (11) the sums in equations Eq. (15) can be reformulated into a recursive form.

$$\begin{aligned} R(n) &= \lambda \cdot \beta(n-1, k) \cdot \sum_{k=1}^{n-1} \phi(k)\phi^T(k) + \phi(n)\phi^T(n) \\ &= \lambda \cdot R(n-1) + \phi(n)\phi^T(n) \\ S(n) &= \lambda \cdot \beta(n-1, k) \cdot \sum_{k=1}^{n-1} \phi(k)y(k) + \phi(n)y(n) \\ &= \lambda \cdot f(n-1) + \phi(n)y(n) \end{aligned} \quad (16)$$

As can be seen when Eq. (16) is substituted in Eq. (14) a recursive formulation for the optimal set of parameters Eq. (10) has been found. According to Ljung in Ref. [1] Eq. (10) can be simplified with some mathematical algebra.

$$\begin{aligned} \hat{\theta}_d(k) &= R(k)^{-1} S(k) \\ &= R(k)^{-1} [\lambda \cdot S(k-1) + \phi(k)y(k)] \\ &= R(k)^{-1} [\lambda \cdot R(k-1) \cdot \hat{\theta}_d(k-1) + \phi(k)y(k)] \\ &= R(k)^{-1} \{ [R(k) - \phi(k)\phi^T(k)] \cdot \hat{\theta}_d(k-1) + \phi(k)y(k) \} \\ &= \hat{\theta}_d(k-1) + R(k)^{-1} \phi(k) [y(k) + \phi^T(k)\hat{\theta}_d(k-1)] \end{aligned}$$

Finally two recursive formulas have been developed which describe the optimal weighted estimate $\hat{\theta}_d$ of the parameter set θ_d which can after estimation been transformed onto the time continuous version of the parameter set θ using Eq. (13).

$$\hat{\theta}_d(k) = \hat{\theta}_d(k-1) + R(k)^{-1} \phi(k) [y(k) + \phi^T(k)\hat{\theta}_d(k-1)] \quad (17)$$

$$R(k) = \lambda \cdot R(k-1) + \phi(k)\phi^T(k) \quad (18)$$

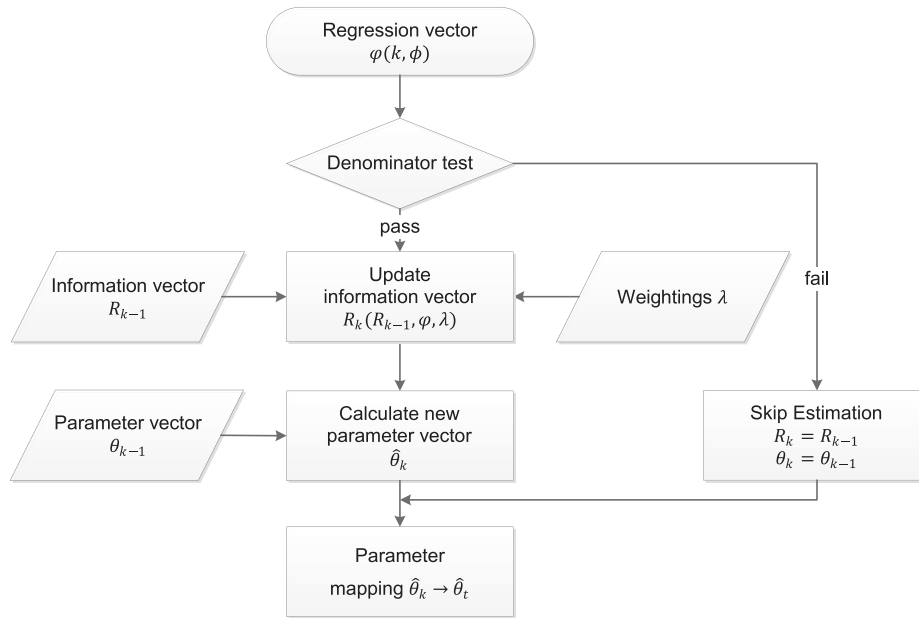


Fig. 1. Flowchart of the weighted recursive least square estimator.

4. Implementation of the weighted recursive estimator for low-cost battery monitoring microcontroller

Because of the recursive formulation, the algorithm described in (17) can be used inside discretely operating systems. Due to the matrix inversion in Eq. (17) numerical stability must be guaranteed. One approach is the use of an efficient matrix inversion lemma which is described in [1].

$$(A + BCD)^{-1} = A^{-1} - A^{-1}B(DA^{-1}B + C^{-1})^{-1}DA^{-1} \quad (19)$$

The Matrix inversion lemma can be applied to (17) by setting $A = \lambda \cdot R(k-1)$, $B = \phi(k)$, $C = \phi^T(k)$ and $D = 1$.

$$R(k)^{-1}\phi(k) = \frac{R(k-1)^{-1}\phi(k)}{\lambda + \phi^T(k)R(k-1)^{-1}\phi(k)} \quad (20)$$

Replacing $R(k)^{-1}\phi(k)$ with (20) in (17) leads to a more efficient formulation of the parameter estimator without the need of a matrix inversion. Instead a division takes place. However for numerical stability of the algorithm it must be ensured that division by zero or very small values do not take place. The denominator must be checked. In case the denominator assumes dangerously low values, the estimation process for this time step will be skipped and the previous value will be used. The entire weighted recursive parameter estimation algorithm is illustrated in Fig. 1.

5. Identification of the current dependency on the charge transfer resistance

The model of the battery cell includes a resistance that describes the charge-transfer process between the electrodes and the electrolyte. The value of the charge-transfer resistance strongly depends on the current that drives the charge-transfer process between the solid electrode phase and the liquid electrolyte. As mentioned in the first paper, the charge-transfer process can be described by the Butler–Volmer equation (BVE) which described the electro-chemical kinetics occurring at the electrode-electrolyte

interfaces. The dependency of the charge-transfer resistance $R_{ct}(I)$ on the current I can be described by the BVE (21).

$$I = A \cdot i_0 \cdot \left[\exp\left(\frac{\alpha_a \cdot F}{R \cdot T} \cdot \Delta U_r\right) - \exp\left(-\frac{\alpha_c \cdot F}{R \cdot T} \cdot \Delta U_r\right) \right] \quad (21)$$

$$R_{ct}(I) = \frac{U_r}{I} \quad (22)$$

To obtain the overvoltage U_r caused by the charge-transfer process for resistance calculation in (22), the BVE has to be solved for U_r . Since the BVE contains two exponential terms which describe the redox reaction occurring at the electrodes, the dependency of the overvoltage U_r on the current I is strongly nonlinear and the BVE (21) cannot simply be solved.

The nonlinear current dependency leads to another aspect that has to be considered during parameter estimation for the equivalent circuit model in Fig. 2. The parameter estimator developed in previous section assumes piecewise linearity of the dynamic behavior of the battery cell under observation. Due to the nonlinear current dependency of the charge transfer resistance caused by the BVE and described in Refs. [3,4,6], the assumption of piecewise linearity of the battery cell does not hold. The current demand on the battery depends on the application, in this case the driving situation of the electric vehicle, and is thus unforeseeable.

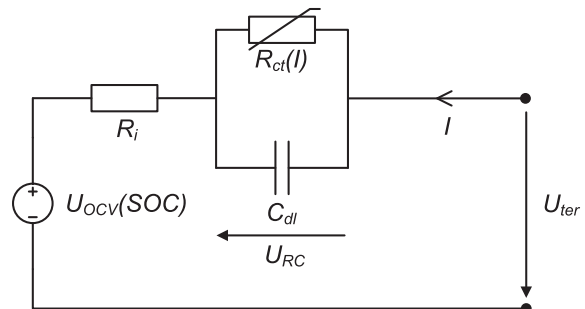


Fig. 2. Equivalent circuit model without diffusion for online parameter estimation.

Moreover the parameter estimator (14) assumes a linear dependency of the voltage on the current at the charge-transfer resistance. The estimated value for R_{ct} thus does not consider the nonlinear dependency due to the BVE.

6. Approximations of the Butler–Volmer equation

It is analytically not possible to directly solve Eq. (21) for the overpotential U_r . The BVE can be simplified with certain assumption. Two assumptions will be presented here and the results of both approximations for Eq. (21) will be compared with each other.

6.1. Assumption of identical cathodic and anodic transfer coefficients

In (21) α_c denotes the cathodic- and α_a the anodic transfer coefficient for which the restrictions (23) and (24) must hold.

$$\alpha_c + \alpha_a = 1 \quad (23)$$

$$\begin{aligned} \alpha_c &> 0 \\ \alpha_a &> 0 \end{aligned} \quad (24)$$

The assumption that α_c is identical with α_a and the restrictions in Eq. (23) and Eq. (24) lead to the conclusion that $\alpha_c = \alpha_a = 0.5$. It is described for example in Refs. [6–8] that the dynamic characteristic of a lithium-ion battery during charge and discharge is quite similar which leads to the conclusion of equal α . However another approximation approach for the BVE which does not require the assumption of equal charge transfer coefficients will be described in the upcoming Section 6.2.

Following the assumption of equal charge transfer coefficient as described in Ref. [6], the following substitutions will be introduced.

$$K = \frac{\alpha F}{RT} \quad (25)$$

This leads to a simplified description of Eq. (21).

$$I = \frac{1}{2} \cdot 2 \cdot A \cdot i_0 \cdot [\exp(K \cdot U_r) - \exp(-K \cdot U_r)] \quad (26)$$

Equation (26) is a hyperbolic sine function, because $\sinh(x) = 1/2 \cdot (\exp(x) - \exp(-x))$ with $x = K \cdot U_r$ and a constant factor. The inverse of the hyperbolic sine function can be applied [9].

$$\sinh^{-1}(x) = \ln(x + \sqrt{x^2 + 1}) \quad (27)$$

Inverting (26) using (27) and substituting the resulting voltage U_r into Eq. (22) leads to the following description of the charge-transfer resistance [6].

$$R_{ct}(I) = R_{ct,0} \cdot \left(\frac{\ln(k_1 \cdot I + \sqrt{(k_1 \cdot I)^2 + 1})}{k_1 \cdot I} \right) \quad (28)$$

The variable k_1 describes the active surface of the electrode A , which is depending on the state of charge and the age of the battery cell as well as the exchange current density i_0 which describes the stiffness of the overpotential of the chemical reaction on the current that drives the charge exchange process [10]. The exchange current density strongly depends on the age and the temperature of the battery and decreases as the battery ages [11].

$$k_1 = (2 \cdot A \cdot i_0)^{-1} \quad (29)$$

6.2. Assumption of neglectable voltage drop at the charge transfer resistance for small currents

Tafel found a first order approximation to describe the dependency of the overpotential at an electrode on the exchange current [12]. This approximation is known as Tafel-equation. The Tafel-equation is valid only for high currents because at high currents the second exponential term in (21) becomes small compared to the first exponential term. Thus it is acceptable to neglect the second exponential term, leading to Eq. (30).

$$I = A \cdot i_0 \cdot \exp\left(\frac{\alpha \cdot F}{R \cdot T} \cdot \Delta U_r\right) \quad (30)$$

Solving Eq. (30) for U_r is straightforward by using the natural logarithm, Eq. (25) and Eq. (29).

$$\begin{aligned} R_{ct}(I) &= \frac{R \cdot T}{|I| \cdot \alpha \cdot F} \cdot \ln\left(\frac{|I|}{A \cdot i_0}\right) \\ &= \frac{1}{K \cdot |I|} \cdot \ln\left(\frac{|I|}{i_0 \cdot A}\right) \\ &= R_{ct,0} \cdot \frac{\ln(2 \cdot k_1 \cdot |I|)}{k_1 \cdot |I|} \end{aligned} \quad (31)$$

It must be noted that the most significant change in the resistances due to the Butler–Volmer equation (BVE) takes place for rather small currents. However the effect remains hardly noticeable because the overall voltage drop is small at small currents. For higher currents, when the voltage drop due to the charge-transfer overpotential becomes significant, the influence of the BVE on the charge-transfer resistance is much smaller. While the assumption of equal α is valid for the entire current range, the Tafel-equation (30) is only valid for high currents and thus the range of high influence of the current on the resistance is neglected. On the other hand Eq. (31) is easier to implement on embedded systems because no square root operation as in Eq. (28) is necessary. That is the reason why both assumptions are used for the investigation of the current-rate influence on the parameter $R_{ct}(I)$ and compared to each other. In case the voltage drop at small currents will be really insignificant, the faster Tafel-equation is used to determine the current influence on the charge-transfer resistance. The overpotential and resistance change caused by the Butler–Volmer kinetics is exemplary shown in Fig. 3.

In both cases however the factor k_1 remains unknown and due to its dependency on the age of the battery cell and temperature it

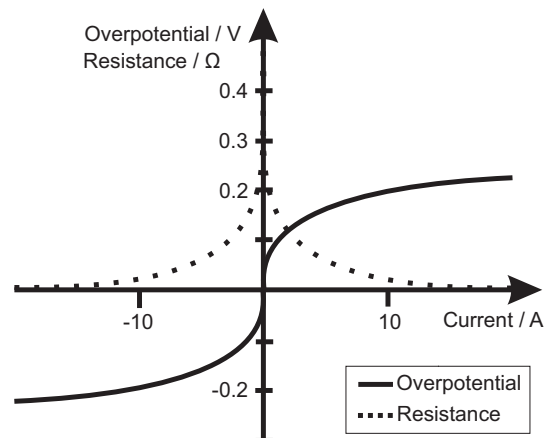


Fig. 3. Overpotential and resistance change caused by the Butler–Volmer kinetics [10].

must be determined to be able to use one of the approximation for the charge-transfer resistance.

7. Nonlinear mutation algorithm

The parameter estimation algorithm described in Section 2 would provide a correct estimation of the charge-transfer resistance R_{ct} assuming a linear dependency of the overpotential at the charge-transfer resistance on the current. In Section 5 a nonlinear dependency has been found. Therefore the estimated $R_{ct,0}$ is only correct for currents around 0 A. The parameter $R_{ct,0}$ must be corrected for higher currents with the derived formula Eq. (28) or Eq. (30) depending on which simplification for the EVE (21) is used. Since the problem is of nonlinear character a suitable approach for estimating the dependency parameter k_i in Eq. (28) and Eq. (30) must be found. Therefore a mutation algorithm is developed which tries to find an optimal k_i for the current operational environment. According to Eq. (29) k_i includes the exchange current density and the active surface which both change in dependency of aging and temperature. Therefore the parameter k_i must be adapted depending on the battery cell's age and temperature.

The algorithm is divided in two parts. Part one consists of a first-in-first-out data queue to collect suitable current- and voltage information online. The second part of the algorithm includes the actual mutation algorithm which operates on the collect data from the queue once enough suitable data is available.

7.1. FIFO-queue and data selection for mutation process

Since the total current is divided between the charge-transfer resistance $R_{ct}(I)$ and the double-layer capacitance C_{dl} it must be assured that the entire current flows over the charge-transfer resistance. Only in that case it is possible to estimate the correct current dependency of the charge-transfer resistance. Alternatively the branch-current flowing over the charge-transfer could be measured but that impossible to measure. Once the capacitance is fully charged all current flowing over the RC-branch will flow through the resistance. It can be assumed that this is the case once a high enough currents remains constant for a certain amount of time [6]. Therefore a current- and voltage measurement is only saved in the queue in case the current is high and steady. For batteries a current rate of 2 C can be assumed as high. This current rate is chosen, because at 2 C the nonlinear effects of the charge-transfer process become visible. Furthermore a current rate of 2 C can be observed during conventional driving cycles [13]. Once sufficient data samples are collected, the set of measurements are handed to the mutation algorithm.

7.2. Mutation algorithm for the determination of the current dependency

Mutation algorithms belong to the class of evolutionary algorithms. They employ recombination, mutation and selection processes for finding an optimal solution to a given problem. They behave much like the biological evolutionary process which gives them their name. Compared to conventional optimization algorithm, algorithms based on evolutionary processes do not require convexity of the problem. This allows the handling of strongly nonlinear and discontinuous optimization problems [14]. Disadvantageous on the other hand is the computational effort necessary to handle huge optimization problems because no analytical solution for the evolutionary process exists. However as described before, only a limited amount of data must be processed in the upcoming optimization problem.

An optimization criterion must be selected for the optimization problem of finding the optimal value of k_i for a given environment of the battery cell. The root mean square error has been found suitable for the optimization problem of finding the optimal linear parameter-set θ in Section 2. It will also be used for this nonlinear optimization problem. The root-mean square error will serve as cost function as described in Eq. (32) and the aim is to minimize the cost function.

$$C_{k_i, BV}(\theta_t, k_i) = \sqrt{\frac{1}{M} \sum_{n=1}^M (U_{pred} - U_{meas})^2} \quad (32)$$

$$U_{pred} = (R_i + R_{ct, k_i}) \cdot I(t) + (R_i R_{ct, k_i} C_{dl}) \cdot \frac{dI(t)}{dt} - (R_{ct, k_i} C_{dl}) \cdot \frac{dU_{RRC}(t)}{dt} \quad (33)$$

The aim therefore is to find a k_i which, in combination with the parameter-set θ_t found with Eq. (17) and Eq. (28) or Eq. (30), reduces the mean root square error $C_{k_i, BV}(\theta_t, k_i)$ to a minimum.

$$\hat{k}_i = \arg \min C_{k_i, BV}(\theta, k_i) \quad (34)$$

Therefore the first step is the calculation of the root mean square error of all data in the queue for the current parameter-set $\theta(t)$ and the current environment-dependency factor $k_i(0)$. The second step is to vary (mutate) the environment-dependency factor randomly with a given precision ξ . Therefore a positive or negative random number with the given precession ξ is added to $k_i(0)$.

$$\hat{k}_i(\xi) = k_i(0) + \xi \quad (35)$$

Afterward the root-mean-square value for all data from the queue is evaluated again for the mutated environment-dependency factor $k_i(\xi)$. This is done by evaluating $R_{ct}(I)$ according to Eq. (31) or Eq. (28). If the root mean square error decreases, the new value $k_i(\xi)$ will be stored (selection). If the error on the other hand increases, the new value $k_i(\xi)$ will be dropped and the previous value will be used instead. The mutation process is repeated until a maximum of iterations is reached. The number of maximal iterations depend on the computing time available. The more iterations are allowed, the higher the precession of the estimated k_i . This ensures that the algorithm convergence towards the correct value of k_i .

A flowchart of the algorithm can be found in Fig. 4 and its results respectively in Fig. 5. Since the current dependency factor k_i only changes with the age of the battery and temperature, it is not necessary to estimate k_i at every moment. The algorithm can therefore work in parallel to the parameter identification technique described in Eq. (17) and provide the current dependency factor k_i for the charge-transfer parameter $R_{ct}(I)$.

8. Diffusion parameter identification

Both diffusion models Eq. (45) and Eq. (46) described in Part 1. can be implemented by means of their state-space representation in a simulation environment. For this, the parameters R_d and C_d must be determined. An online identification as developed before for the charge-transfer process is not feasible because the relevant frequencies at which the diffusion process occurs are in the range of some mHz as can be seen in the impedance spectrum Fig. (7) in the first paper. The diffusion process needs to be excited with an excitation signal of corresponding frequency. The time for one period of an excitation at such low frequency can easily reach several minutes. In impedance spectroscopy the diffusion process is also the one that needs most of the measuring time. Therefore an

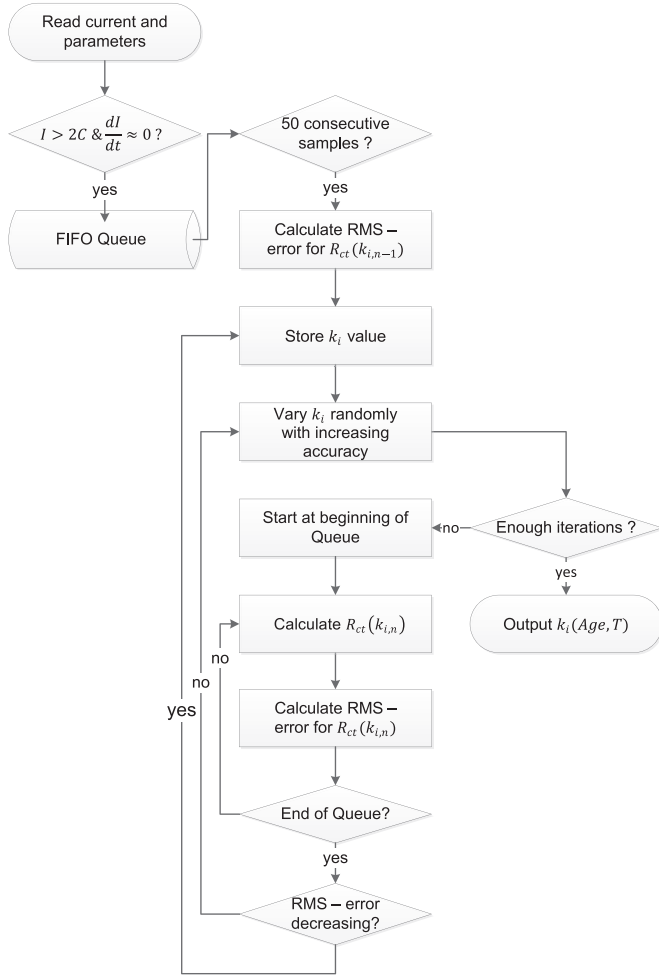


Fig. 4. Flowchart of the mutation based nonlinear current dependency estimator.

online identification of the process is not necessary because of the high time constant of the diffusion process. The identification of the diffusion process state-space model parameters is conducted off-line or in parallel to the operation of the battery after enough data for a parameter identification has been collected.

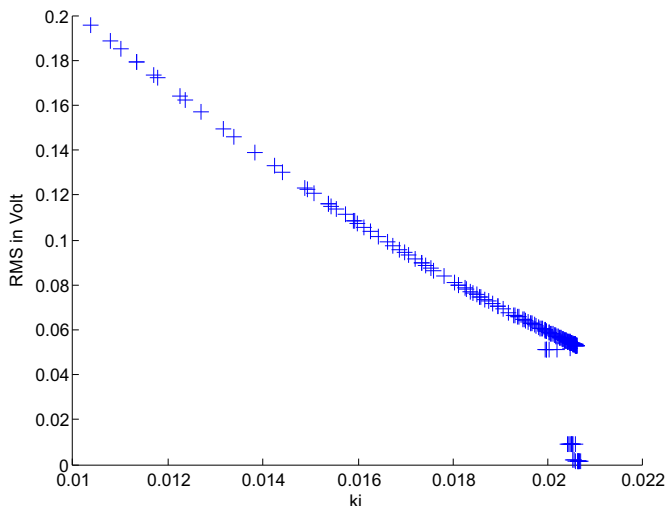


Fig. 5. An exemplary example of results for the k_i estimation.

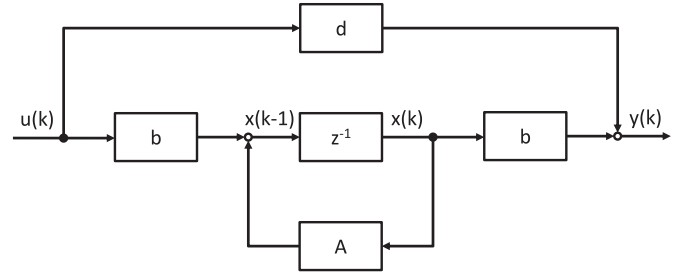


Fig. 6. Discrete time state-space system.

8.1. Grey-box system identification approach

In the first paper a model for the diffusion process has been found. Its state-space representation Eqs. (45) and (46) specifies the mathematical structure of the underlying diffusion process by means of a system of differential equations. The state-space representation links the unknown parameters R_d and C_d with the input and output of the system and implements them in a mathematical construct of several differential equations. Thus the state-space representation can serve as a Grey-box model as it has been introduced by Ljung in Ref. [1]. A black-box model in contrast would provide no underlying mathematical construct for the underlying physical process and the system of differential equations could be freely specified.

For each Warburg-impedance approximation a grey-box model has to be created. They contain the ordinary differential equation set with identifiable parameters R_d and C_d as a state-space model. Furthermore the state-space system is transformed into the discrete-time domain. The discrete time state-space system is shown in Eq. (36) and Fig. 6.

$$\begin{aligned} \mathbf{x}(k+1) &= \mathbf{A}\mathbf{x}(k) + \mathbf{b}u(k) \\ y(k) &= \mathbf{c}\mathbf{x}(k) + \mathbf{d}u(k) \end{aligned} \quad (36)$$

The discrete time state-space matrices \mathbf{A} , \mathbf{b} , \mathbf{c} , \mathbf{d} can be derived from the corresponding continuous time Warburg state-space model Eq. (45) and Eq. (46). Let \mathbf{F} , \mathbf{g} , \mathbf{h} , \mathbf{k} be the continuous time state-space matrices of the Warburg impedance model and T denotes the discrete time step, then the discrete state-space matrices can be derived as follows [15]

$$\begin{aligned} \phi(t) &= e^{\mathbf{F}t} \\ \mathbf{A} &= \phi(T) \\ \mathbf{b} &= \int_{kT}^{(k+1)T} \phi(\tau) \cdot \mathbf{g} \, d\tau \\ \mathbf{c} &= \mathbf{h} \\ \mathbf{d} &= \mathbf{k} \end{aligned}$$

The discrete time grey-box model can now be used for identification of the underlying diffusion process. Therefore a set of collected data of sufficient length as discussed before is used where the recorded current serves as input $u(k)$ and the voltage that cannot be described by the charge-transfer process described in Eq. (2) and the open-circuit voltage as described in 12.1 serves as output $y(k)$. The error-voltage is available because before an error term $e(k)$ has been introduced. All dynamics that cannot be explained by Eq. (17) are mapped on this parameter. They are the open-circuit voltage and the voltage drop caused by the diffusion process. In Section 12.1 a method for determination of the open-circuit voltage is introduced. The resulting open-circuit voltage is subtracted from the error term $e(k)$ which leaves a voltage drop

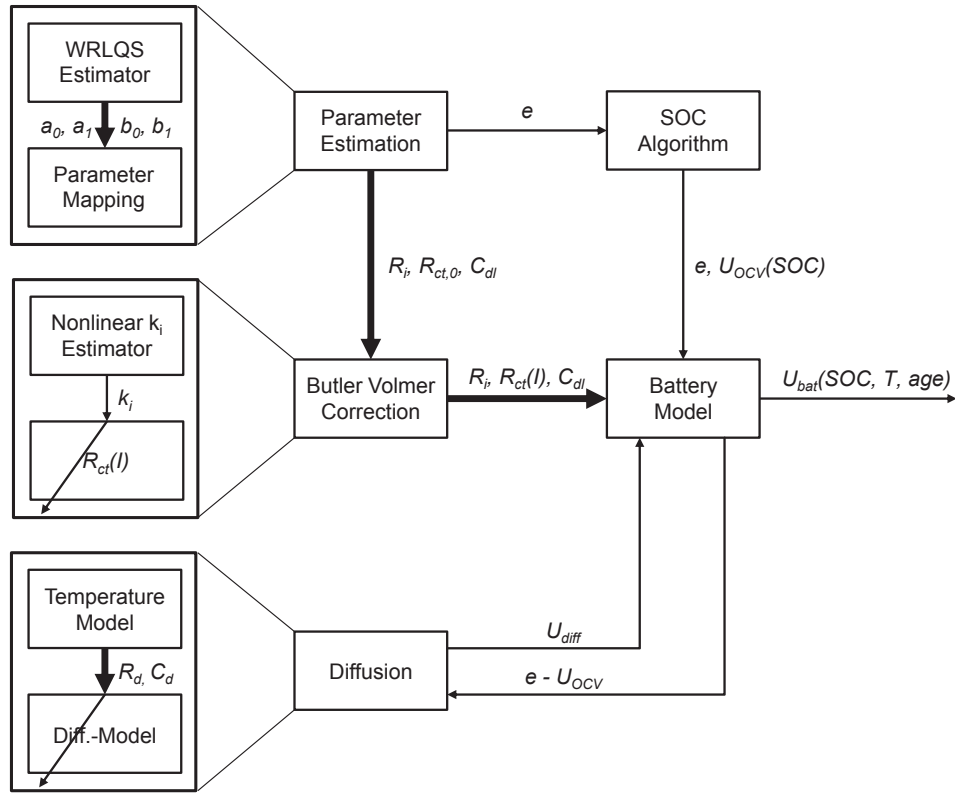


Fig. 7. Overall parameter estimation regime.

mainly caused by the diffusion process that can be used for the identification of the diffusion model parameters.

$$y(k) = U_{\text{diffusion}} = e(k) - U_{OC} \quad (37)$$

The system identification is conducted using a subspace algorithm described in detail in Ref. [1], which employs a least-square approach as described in Section 2 is used to fit the state-space matrices **A**, **b**, **c**, **d** to the collected input and output samples. According to Ljung in Ref. [1] the state-space system can be rewritten as shown in Eq. (38).

$$\begin{aligned} \mathbf{Y}(k) &= \begin{Bmatrix} \mathbf{x}(k+1) \\ y(k) \end{Bmatrix} \\ \Theta &= \begin{Bmatrix} \mathbf{A} & \mathbf{B} \\ \mathbf{C} & \mathbf{D} \end{Bmatrix} \\ \Phi(k) &= \begin{Bmatrix} \mathbf{x}(k) \\ u(k) \end{Bmatrix} \\ \mathbf{Y}(k) &= \Theta \cdot \Phi(k) \end{aligned} \quad (38)$$

Eq. (38) has the form of a linear regression according to Ljung in Ref. [1]. The elements of Θ can be estimated using a least square method [1]. Constraints define the relationship of the state-space coefficients in the system matrices **A**, **b**, **c**, **d**. The structure of the differential equations described by the system matrices of the state-space system influence the optimization process as side conditions. As a result we obtain the system matrices **A**, **b**, **c**, **d** from which the parameters R_d and C_d can be extracted using Eqs. (39) and (40) which were derived in our first paper.

The state-space model can then be implemented in the simulation environment using a discrete time state-space model as shown in Fig. 6.

8.2. Temperature dependency of the diffusion parameters

As described in the first paper, the temperature significantly influences the diffusion process. As it is not possible to predict the parameters online, the offline predicted parameters are only valid for the temperature at the time of the recording of the current- and voltage data that has been used for the offline parameter estimation. Assuming the temperature has changed between two operations of the battery cell, the diffusion model will produce errors because the estimated parameters are not valid for the current temperature.

To circumvent this error, a temperature model is introduced to adjust the parameters for new battery temperatures. Therefore the definition of the diffusion parameters in the first paper with Eqs. (39) and (40) as given by Ref. [16] is recalled.

$$R_d = \frac{l \cdot R_{\text{gas}} T}{D \cdot cn^2 F^2 A_e} \quad (39)$$

$$C_d = \frac{l \cdot cn^2 F^2 A_e}{R_{\text{gas}} T} \quad (40)$$

with l denotes the diffusion length. The parameter A_e denotes the active surface of the electrode which changes with the age of the battery. Furthermore the parameter T denotes the temperature and parameter D describes the diffusion coefficient which is a function of temperature. The diffusion coefficient in solid materials such as the electrodes is governed by solid state diffusion [17].

$$D = D_0 \cdot \exp\left(-\frac{E}{R_{\text{gas}} T}\right) \quad (41)$$

During each estimation process, the mean temperature T_{ref} during which the sampling data has been recorded is saved as reference temperature together with the diffusion parameters. Before the parameters are handed over to the diffusion model, they are adapted to adjust the temperature difference between T_{ref} and the current temperature T_{now} . Eqs. (39) and (40) derived in the first paper both show a linear dependency on the temperature. Furthermore the diffusion resistance also depends on Eq. (41) which can be reformulated to adjust the temperature difference.

$$\frac{D_{T_{\text{ref}}}}{D_{T_{\text{now}}}} = \exp\left(-\frac{E}{R_{\text{gas}}} \cdot (T_{\text{ref}}^{-1} - T_{\text{now}}^{-1})\right) \quad (42)$$

The constant R_{gas} again stands for the universal gas constant, however E stands for the energy barrier of the diffusion process. In Ref. [18] an energy barrier for the lithium ion movement of 20 kJ mol^{-1} to 40 kJ mol^{-1} has been predicted. Setting the energy barrier in the temperature model to 20 kJ mol^{-1} produces the smallest error for all tested configurations. Using Eq. (42) and the linear temperature dependency on Eqs. (39) and (40) from the first paper results in the following temperature dependency.

$$R_{d,T_{\text{now}}} = R_{d,T_{\text{ref}}} \cdot \frac{T_{\text{now}}}{T_{\text{ref}}} \cdot \exp\left(-\frac{E}{R} \cdot (T_{\text{ref}}^{-1} - T_{\text{now}}^{-1})\right) \quad (43)$$

$$C_{d,T_{\text{now}}} = C_{d,T_{\text{ref}}} \cdot \frac{T_{\text{ref}}}{T_{\text{now}}} \quad (44)$$

These temperature adjusted parameters are fed into the two state-space models for the diffusion process Eqs. (45) and (46) derived in the first paper.

$$U_d = \{1 \ 0 \ 0 \ \dots \ 0 \ 0 \ 0\} \cdot \mathbf{U}_c + \frac{R_d}{N} \cdot I$$

$$\dot{\mathbf{U}}_c = \frac{N^2}{R_d \cdot C_d} \begin{Bmatrix} -1 & 1 & 0 & \dots & 0 & 0 & 0 \\ 1 & -2 & 1 & \dots & 0 & 0 & 0 \\ \vdots & \vdots & \vdots & \ddots & \vdots & \vdots & \vdots \\ 0 & 0 & 0 & \dots & 1 & -2 & 1 \\ 0 & 0 & 0 & \dots & 0 & 1 & -1 \end{Bmatrix} \cdot \mathbf{U}_c + \frac{N}{C_d} \begin{Bmatrix} 1 \\ 0 \\ \vdots \\ 0 \\ 0 \end{Bmatrix} \cdot I \quad (45)$$

$$U_d = \{1 \ 1 \ 1 \ \dots \ 1 \ 1 \ 1\} \cdot \mathbf{U}_c$$

$$\dot{\mathbf{U}}_c = \frac{1}{R'_d \cdot C'_d} \begin{Bmatrix} -1 & 0 & 0 & \dots & 0 & 0 & 0 \\ 0 & -1 & 0 & \dots & 0 & 0 & 0 \\ \vdots & \vdots & \vdots & \ddots & \vdots & \vdots & \vdots \\ 0 & 0 & 0 & \dots & 0 & -1 & 0 \\ 0 & 0 & 0 & \dots & 0 & 0 & -1 \end{Bmatrix} \cdot \mathbf{U}_c + \frac{1}{C'_d} \begin{Bmatrix} 1 \\ 1 \\ \vdots \\ 1 \\ 1 \end{Bmatrix} \cdot I \quad (46)$$

It is therefore now possible to record the diffusion estimation data at a different temperature and adjust the resulting parameters so that they still keep valid for other temperatures ranges. In the upcoming chapter the results of this temperature model are discussed in detail. The overall parameter estimation regime is illustrated in Fig. 7.

8.3. Verification of the parameter identification algorithm

Before the proposed parameter identification algorithm shown in Fig. 7 can be used to determine the states of the battery, the

estimated parameters have to be verified. First it has to be determined which approximation for the BVE shall be used. Two driving cycles are used and the error of both models is evaluated to determine the best approximation. Furthermore the diffusion model used for determining the diffusion voltage drop has to be verified too. Afterward the results of the complete parameter identification algorithm are compared against the results from impedance spectroscopy and a pulse-test is conducted to verify the correctness of the estimated parameters.

8.4. Comparison of the approximations of the Butler–Volmer equation

Before two possible approximations for the BVE in Eq. (21) have been introduced. The first is based on the assumption of equal cathodic and anodic transfer coefficients. This assumption is valid for all current-rates. The second assumption bases on the Tafel equation. It assumes that the voltage drop at the charge-transfer resistance is negligible for small currents as mentioned in Section 6.2. The second assumption poses a harder limit on the algorithm because it can only work at high currents. On the other hand the second assumption removes a square-root operation from the algorithm which lowers calculation time. Therefore it is interesting to see if the second assumption could also be used for determination of the nonlinear charge-transfer characteristic.

For both approximations the root mean square error is recorded during a typical mixed driving cycle as shown on the top of Fig. 8. The battery cell used for this test is cell K-2, a Kokam 40 Ah cell which has aged to a remaining capacity of 38 Ah and which is operated at 0°C . The parameter identification is conducted without the diffusion model because it relies on a correct estimation of the high dynamic voltage drop. The root mean square error is calculated according to Eq. (47). The advantage of using the root mean square error is its ability to proof that the estimator is stationary stable. If the root mean square error does increase further and further the estimator does not provide a stable estimate.

$$\text{RMS} = \sqrt{\frac{\sum_{t=1}^n (U_t - \hat{U}_t)^2}{n}} \quad (47)$$

The resulting error is shown at the bottom of Fig. 8. Both approximations result in a lower average error and their stationary behavior is stable because the error is not increasing indefinitely. However the assumption of equal transfer coefficients $\alpha_a = \alpha_c = 0.5$ results in a better approximation of the measured voltage and thus a smaller average error, as it has been expected. To investigate the reason for the deviation between both approximations a closer look is taken at a time interval with high current demand peaks as shown in Fig. 9. It can be seen that the Tafel-equation approximations results in higher drops of the charge-transfer resistance during high current peaks than the assumption of equal transfer coefficients. Furthermore the Tafel-equation is only valid for high absolute currents. As a result of high current tests on a Kokam 40 Ah battery cell, a current of 2 C (80 A) is considered high. The assumption of equal transfer coefficients on the other hand is valid for all current-rates. Most likely this is the main reason why the assumption of equal transfer coefficients provides a better result.

The Tafel equation can be used for batteries that do not allow the assumption of equal transfer coefficients. In all other cases the assumption of equal transfer coefficients produces better results.

9. Comparison of the diffusion model implementations

Two possible state-space implementations of the diffusion model have been introduced in the first paper and recalled in Eqs.

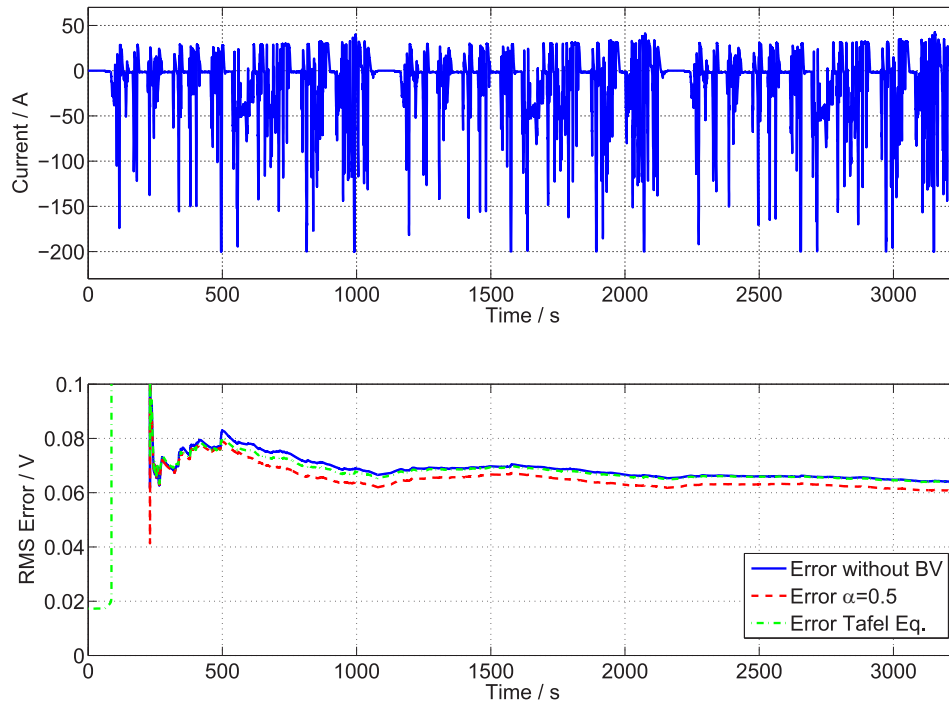


Fig. 8. Root mean square error of both approximations of the Butler–Volmer equation.

(45) and (46). For the evaluation of both diffusion models a high current demanding driving cycle is used. The battery cell under investigation is a new Kokam 40 Ah battery operated at 25 °C. The results of the diffusion parameter identification using the greybox state-space identification technique described earlier are presented in Fig. 10. It can be seen that the porous electrode model results in a lower diffusion resistance R_d , while the diffusion capacitance C_d is estimated higher than the parameter from the inverse-Laplace model. The resulting root-mean-square error is shown in Fig. 10.

Both models lead to a smaller average error compared to the error without the use of a diffusion model. However especially at high current rates the porous electrode model shows a significantly lower average error. A close up at a high current demanding part of the driving cycle shows that the porous electrode model can follow the terminal voltage of the battery. The reason for this behavior might be found in Ref. [19]. The model b) in Fig. 11 from the first paper is correct if the model contains an open-circuit voltage source. The open-circuit voltage source shows a differential

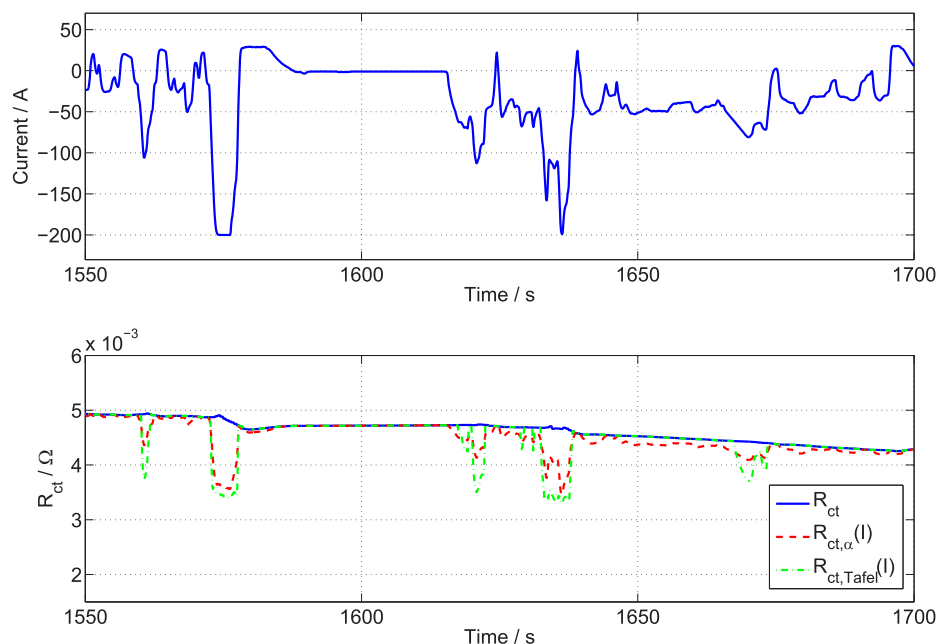


Fig. 9. Course of charge-transfer resistance with different approximations for the Butler–Volmer equation.

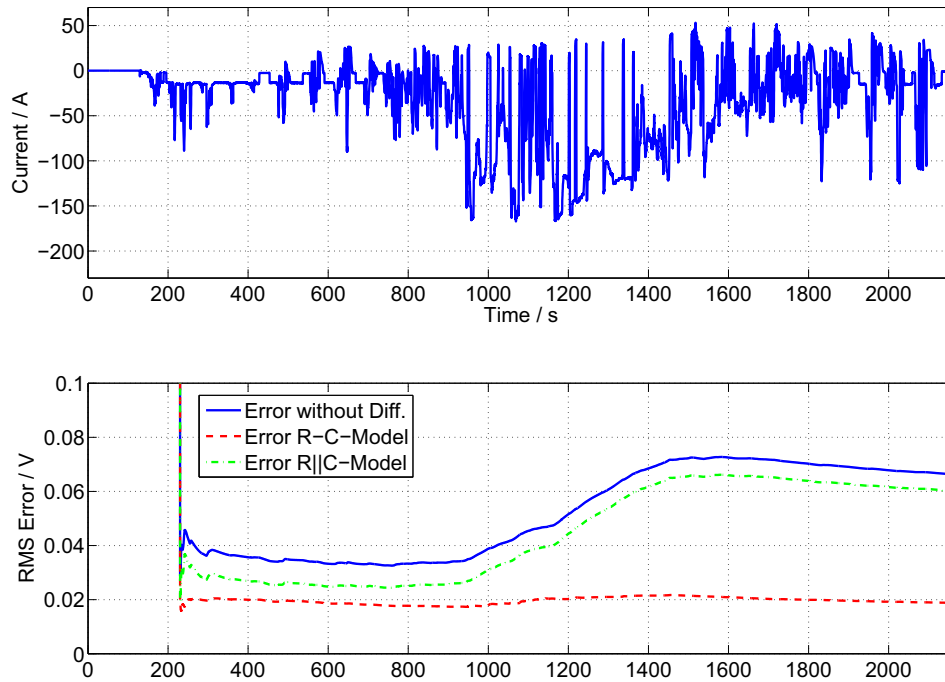


Fig. 10. Error comparison of both diffusion models.

behavior like a capacitance. If the model and the open-circuit voltage is combined, the resulting spectrum will look like the spectrum of model c) in Fig. 11 from the first paper.

10. Verification by impedance spectroscopy

The identified parameters can be compared to the results of a verified method for parameter identification. Such a method is the impedance spectroscopy as described in the first paper. The

spectrum of the voltage response of the battery on a frequency changing current signal is recorded in a Nyquist plot. Several parameters, especially the resistances, can be directly read from the spectrum in the Nyquist plot. The point where the spectrum crosses the real axis marks the value of the serial resistance. The first visible semicircle represents the charge-transfer process between the electrodes and the electrolyte. The charge-transfer resistance R_{ct} can be determined by measuring the length of the semicircle [20]. The results of the analysis of the spectrum of a new Kokam 40 Ah

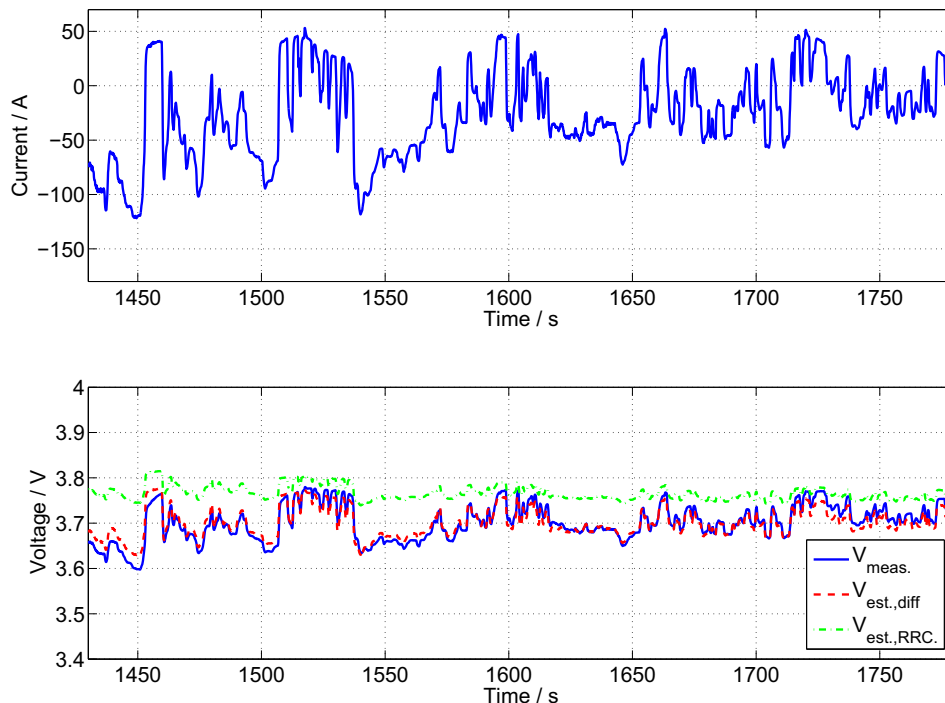


Fig. 11. Comparison of voltage estimation of both diffusion models.

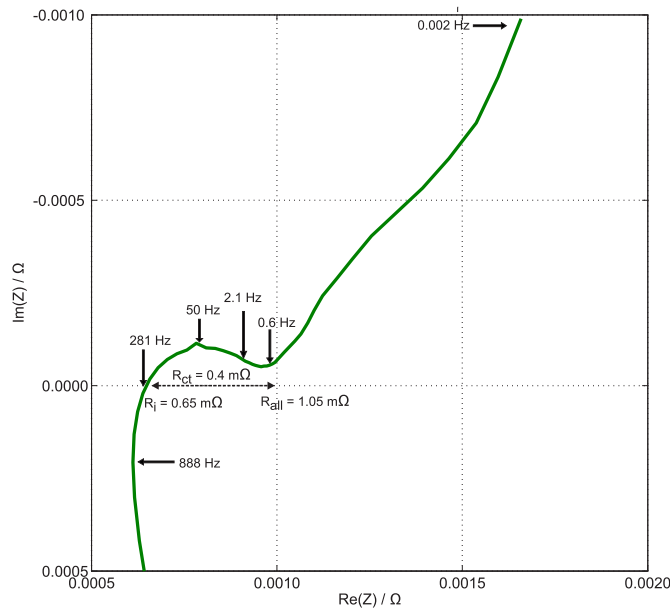


Fig. 12. Impedance spectrum at 25 °C.

cell operated at different temperatures are presented in Figs. 12 and 13. They show that the inner resistance R_i does change as function of the temperature. In contrast, the charge-transfer resistance R_{ct} experiences a significant increase from 0.4 mΩ to 1.4 mΩ which results in an increase of the overall resistance R_{all} .

To compare the results the estimation method described earlier is used to identify the parameters of the battery model. In contrast to impedance spectroscopy the battery is operated under a conventional driving cycle current profile instead of a predefined frequency changing current signal as it is done for impedance spectroscopy. The reason is that the frequency changing sinusoidal current signal of impedance spectroscopy does not occur under normal operating conditions of a vehicle battery. However it is still

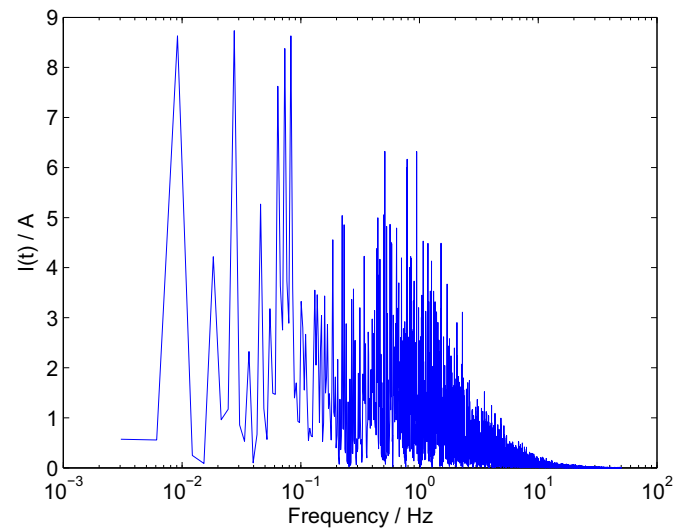


Fig. 14. Frequency analysis of the city driving profile current signal.

necessary to proof that the estimation results reflect the physical properties as determined with impedance spectroscopy.

The signal and the online estimated resistances R_i and R_{ct} are shown in Fig. 15. Again a new Kokam 40 Ah battery cell is used at different temperatures. The results for the new Kokam battery cell reflect the same development as shown in impedance spectroscopy. The charge-transfer resistance R_{ct} at 25 °C increases from a mean of 0.75 mΩ to 1.4 mΩ at 10 °C. The inner resistance R_i increases from 0.45 mΩ to 0.7 mΩ. The overall resistance R_{all} is 1.2 mΩ at 25 °C and 2.1 mΩ at 10 °C. Although the distribution of the overall resistance is not the same as expected by impedance spectroscopy, the overall resistance R_{all} is estimated correctly.

10.1. Frequency spectrum of a city driving cycle

The reason for the wrong distribution of the overall resistance can be found in the frequency analysis of the current signal of the driving cycle. While a huge part of the spectrum is used for the input current signal at impedance spectrum (namely 2 mHz to more than 1 kHz), only a limited part of the spectrum (namely 0.01 Hz–10 Hz) can be found in the current signal of a normal city driving cycle as shown in Fig. 14. The reason is that the main current demand is requested from the power train of the electric vehicle and its dynamics are determined by the operation of the vehicle [21]. It means that during driving operation there are no dynamics that are faster than 0.1 s. To determine the exact value of the inner resistance R_i for example, it is necessary to excite the battery with a frequency that corresponds to the $\text{Im}(Z) = 0$ point in the Nyquist-diagram. In Fig. 12 that point can be reached by exciting the battery with a sinusoidal current signal of 281 Hz. That is outside the frequency range of the current signal that is recorded during city-driving operation. Therefore it is difficult to reproduce the exact distribution for the resistances as given in impedance spectroscopy [22]. However, the overall resistance of the battery cell is correct as can be seen in Fig. 15. The overall resistance R_{all} estimated by the online parameter identification technique can be used to evaluate physical properties of the battery cell since the results are reproducible by impedance spectroscopy. Because R_{all} contains the charge-transfer resistance R_{ct} , which is a function of age and temperature, the parameter can be used to identify the battery state of health. [16].

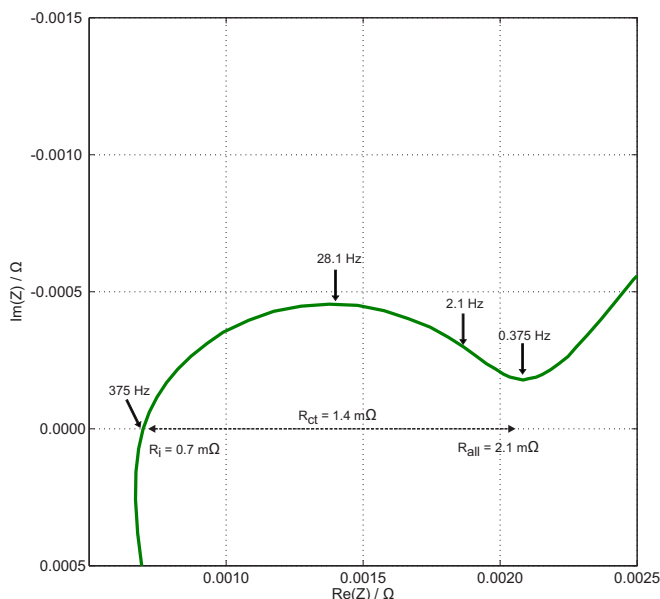


Fig. 13. Impedance spectrum at 10 °C.

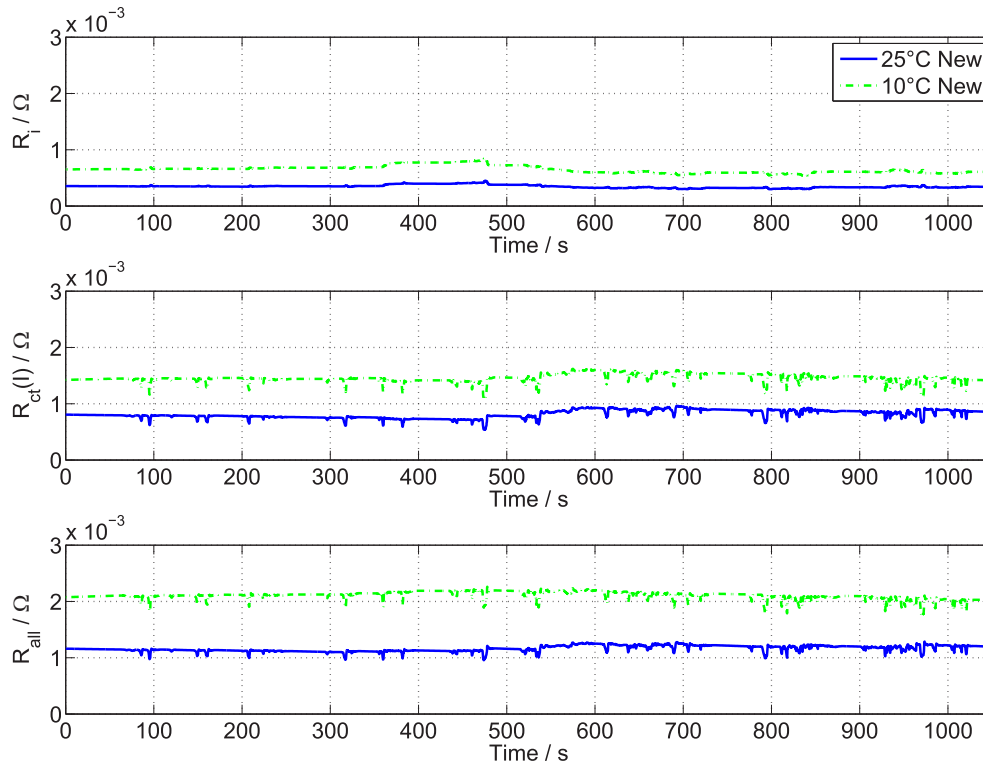


Fig. 15. Identified resistances for a new Kokam 40 Ah lithium-ion battery cell.

11. Verification by current pulse test

Besides impedance spectroscopy it is possible to determine the overall resistance of the battery by applying a pulse current signal on the battery and evaluating the resulting voltage response. The resulting resistance of the battery can be calculated using Ohms law.

$$R = \frac{\Delta U}{|I|} \quad (48)$$

Furthermore the battery model can be verified by comparing the voltage response of the actual battery and the battery model running with identified parameters. To verify the proposed diffusion-model, the voltage response of a battery model with the diffusion model and the voltage response of a battery model without the diffusion model are compared to each other. The battery under test is Cell K-1, a new Kokam 40 Ah lithium-ion NMC-battery cell operated at 25 °C. The pulse signal shown at the top of Fig. 16 is repeated until the battery reaches the end of discharge.

The voltage response and the root-mean-square error calculated according to Eq. (47) are presented in Fig. 16. It becomes obvious that the proposed battery model is well suitable to follow the voltage response of the battery cell. Furthermore the inclusion of the diffusion model further reduces the estimation error by allowing the battery model to follow the huge voltage drops at high current peaks more precisely. Two more observation can be made from the current profile in Fig. 16. During the first current pulse cycle it is not possible to charge the battery with the maximum current peak of 100 A. The reason is that the battery is already at full charge and further charging would increase the terminal voltage of the battery to unsafe levels of above 4.2 V. The battery shows a weak state of function for charge operation. The same applied to discharging occurs during the last current cycle.

The battery cannot be discharged with the long discharge current pulse because it would lower the terminal voltage to unsafe voltages of below 2.7 V. The estimated results are presented in Fig. 18. It is noticeable that at higher depth of discharge more heat during discharge is produced. The reason can be found in an increase of the charge-transfer resistance during discharge. Towards the end of discharge the charge-transfer resistance has increased by about 40% as can be seen by the median value shown in Fig. 19. This behavior has been reported in literature as for example in Ref. [23]. Furthermore the increase of the charge-transfer resistance can also be observed in impedance spectroscopy. The increase of the charge-transfer resistance is correlated with the decrease of the state-of-charge.

The resistance of the battery cell can be evaluated by measuring the voltage drop at a sufficiently high current pulse. The so called direct current resistance should approximately be of the size of the total cell resistance [22].

$$R_{DCR} = \frac{U_{drop}}{I_{pulse}} \quad (49)$$

A pulse is taken from the pulse current profile discussed before. The voltage drop is determined to be $U_{drop} \approx 0.11$ V. The absolute value of the current is determined to be $I_{pulse} = 60$ A. Using Ohms law the resulting direct current resistance is evaluated to be $R_{DCR} = 1.83$ mΩ. This coincide with the estimated overall resistance of $R_{all} = 1.9$ mΩ as can be seen in Figs. 18 and 17 at time 4400 s.

12. State determination of the battery cell

The identified parameters of the battery cell can be used to evaluate the state of the battery cell. If the states of all cells are known it will be possible to evaluate the state of the entire battery and to identify faulty battery cells. The state of charge, state of health and state of function are of interest for assessing the

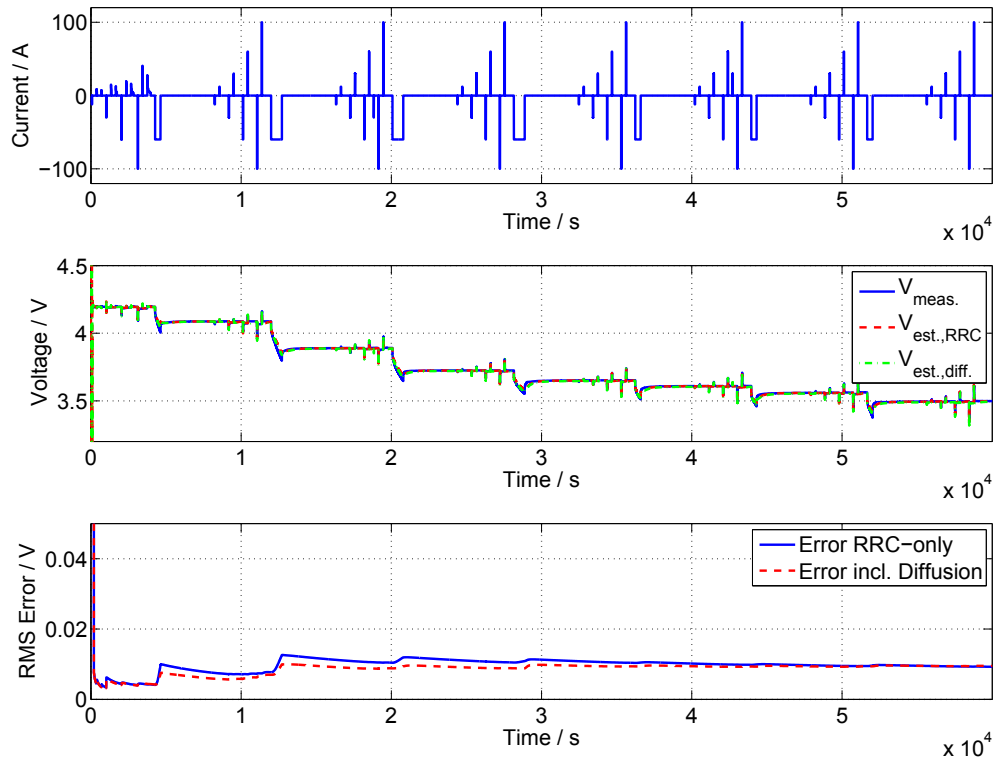


Fig. 16. Voltage response and estimation error during pulse discharge.

functionality of the battery. Therefore in this chapter methods will be defined to determine the above mentioned states with the parameters identified by the parameter identification techniques described earlier.

12.1. State of charge determination

A promising approach for the determination of the state of charge is based on current integration. In the continuous time

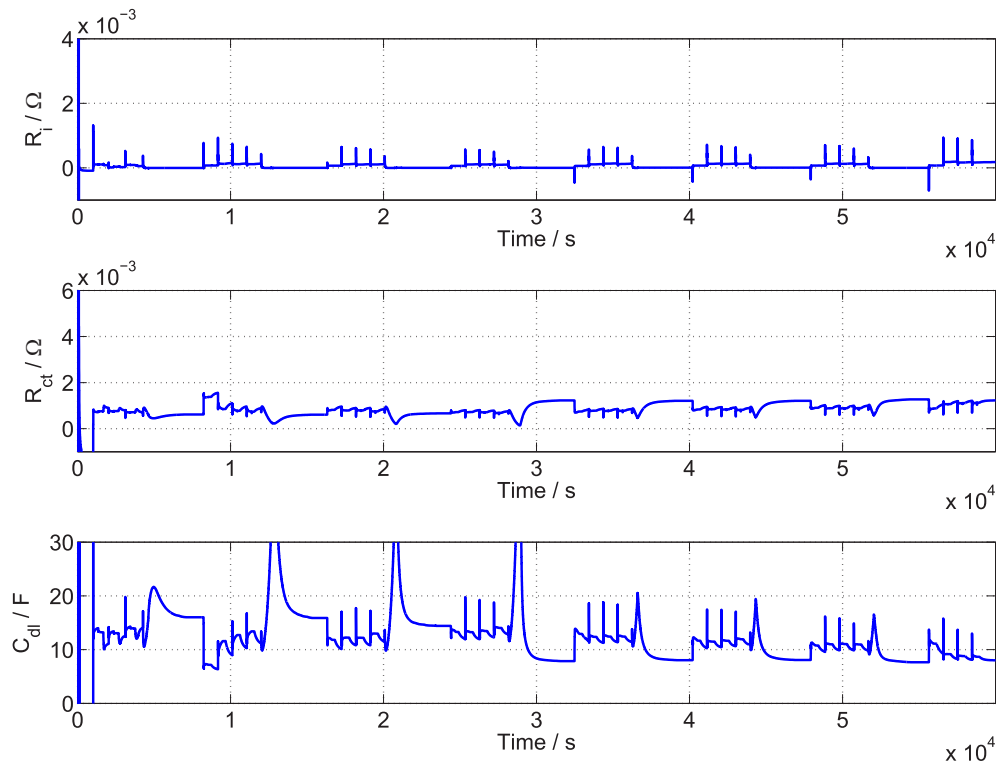


Fig. 17. Estimated parameters for the battery model.

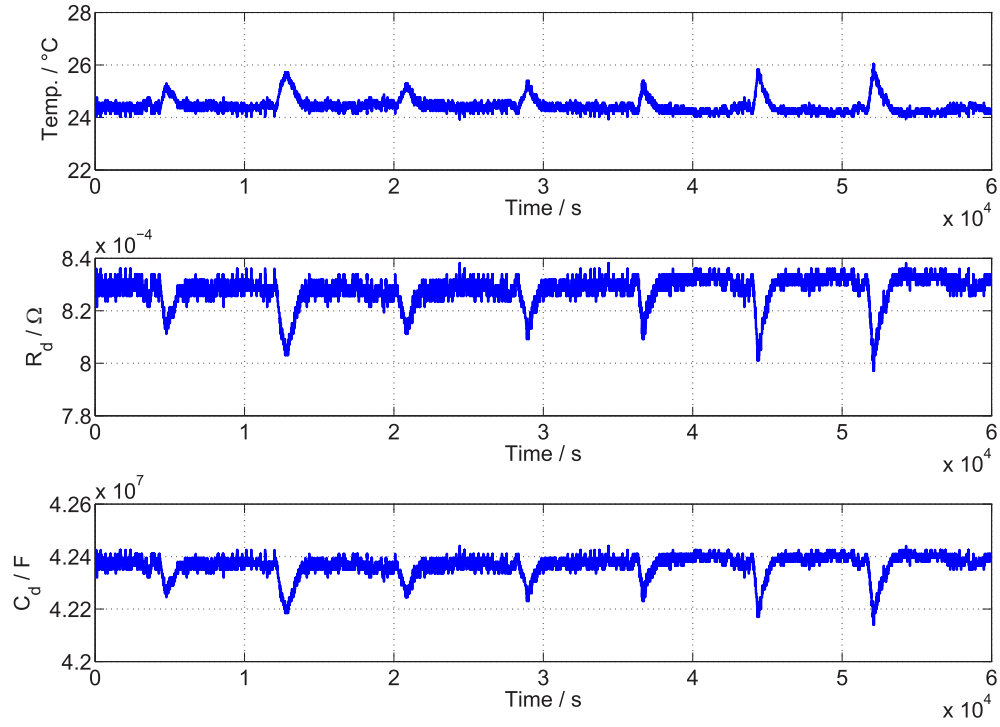


Fig. 18. Estimated parameters for the battery model.

domain the state of charge can be determined using Eq. (50) where C_{act} denotes the actual capacity of the battery cell given in

$$SOC = SOC_0 + \frac{100}{C_{act}} \cdot \int_{t_0}^t I_{flow} d\tau \quad (50)$$

The integral-relation equation can be transformed into the time discrete domain by replacing the integral with a zero-order-hold element.

$$SOC_k = SOC_{k-1} + I_{flow} \cdot \frac{100 \cdot T_s}{C_{act}} \quad (51)$$

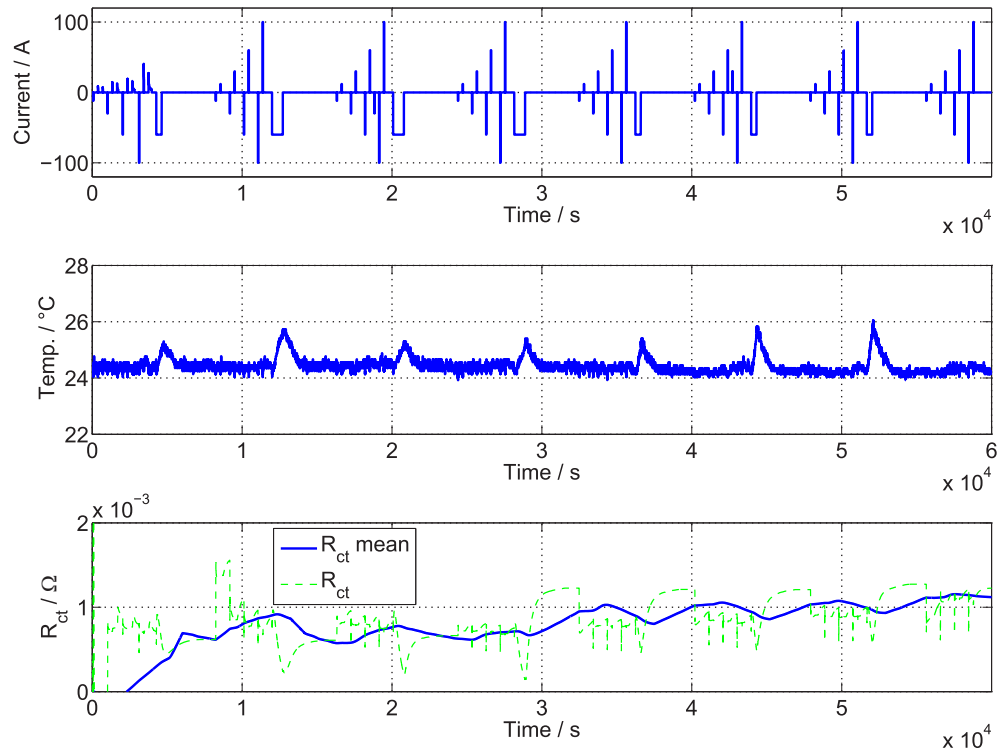


Fig. 19. Increase of charge-transfer resistance during discharge.

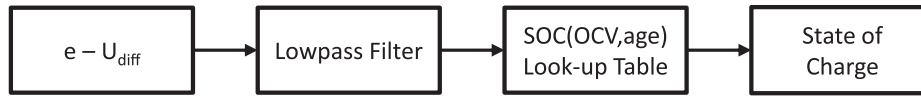


Fig. 20. State of charge determination based on the error-term of the parameter identification.

Note that T_s denotes the time step. It becomes obvious that Eq. (51) is a recursive formula because only the previous value of the state of charge SOC_k is needed. Still for $k = 1$ an offset value SOC_0 is needed. Two options are available to obtain the offset value. First it can be assumed that after a full charge the battery cells state of charge is at 100%, thus $SOC_0 = 100\%$. If a certain offset value for the initial state of charge cannot be assumed, an offset-error occurs which results in a wrong state of charge. This offset-error cannot be correct by the coulomb-counting algorithm. Therefore, the error term e of Eq. (3) that includes the non-identifiable dynamics of Eq. (17) can be used after the parameter estimator has reached a steady state condition to identify the offset. This normally occurs after some seconds at $t = t_{steady}$. Furthermore the diffusion overpotential U_{diff} must be subtracted from the error term to remove the influence of the mass transport process.

$$U_{SOC_0} = e(t_{steady}) - U_{diff}(t_{steady})$$

This procedure is possible because the parameter estimator Eq. (17) maps all charge-transfer and double-layer dynamics on the parameter-set of the simplified battery model. Furthermore the state of charge counter can also be recalibrated during operation. This is possible when the battery reaches a steady-state, for example after a period of zero current. The error term in this case only includes the electromotive force. Because the influence of diffusion is given by U_{diff} , the open-circuit voltage can roughly be obtained by $U_{OC}(t) = e(t) - U_{diff}(t)$. Since the error-term e can only provide a voltage, a nonlinear look-up table that incorporates the transformation between the open-circuit voltage and the state of charge is used to obtain the state of charge as illustrated in Fig. 20 [24]. High dynamic overpotentials are removed by a low-pass filter. Such high dynamic overpotentials might occur due to unmodeled processes such as the charge transfer through the solid electrolyte interface or inaccuracies in the used battery model. A comparison of both state of charge filters illustrated in Figs. 20 and 21 reveals that the coulomb-counter based state of charge determination works very robust (Fig. 23). That has been expected because measurement errors are filtered out due to their white noise characteristic. Under a low current-rate characteristic both state of charge filters behave similar. Under a high current-rate characteristic however the state of charge estimated by the error-term technique is slightly higher than the state of charge estimated by the coulomb-counter. The result of a drive-cycle with high current demands is shown in Fig. 23. The reason is that the diffusion model does not incorporate all diffusion characteristics and thus an overpotential still remains on the error. Both filters work in parallel and during low current demand the coulomb-counter filter can be re-calibrated using the error-term based state of charge filter. The open-circuit voltage U_{OC} can be obtained by the inverse of the look-up table used in 20. The full state of charge determination regime is illustrated in Fig. 22.

12.2. State of health determination

As mentioned earlier the state of health reflects the aging process of the battery cell. Bohlen et al. used impedance spectroscopy to track the change of impedance caused by aging of the battery [20,26,27]. Especially the high-frequency resistance is increasing [4]. They state that the reason for that is an increase in resistance between the current collector and the active mass at the positive electrode. Therefore keeping track of the resistance can be used to determine the state of health. It is also possible to state the remaining useful life of the battery [20,28]. However this definition does not account for calendric aging of the battery and it is rather vague.

Two options are left to define the state of health. First it can be defined as the remaining capacity of the battery. The second option is to define the state of health as the increase in battery-resistance. The increase in resistance causes a higher temperature increase during operation which effects the usability of the battery. Especially if single battery cells in a battery pack are considered, it is important to identify the cells, that show an increase resistance because they limit the power capability of the entire battery pack. Furthermore, the heat production of the battery cell is proportional with the cell resistance. For thermal considerations it is advantageous to know which cell shows an elevated resistance. Therefore a decrease in the state of health in this thesis is defined as an increase of the resistance of the battery or a cell of it to a certain level. According to Bohlen in Ref. [20] especially the charge-transfer resistance R_{ct} is supposed to experience a significant increase for aged batteries. In order to verify the capability of state of health tracking of the proposed parameter identification technique two experiments are carried out. Most important is the permanent observation of the state of health of each battery cell during the operation of the battery for example in an electric vehicle. An increase in resistance causes a temperature increase which endangers safe operation of the battery especially under high current demand.

Fig. 25 shows the temperature characteristic of cell K-1 and cell K-2. Both battery cells are exposed to a high current demanding driving cycle with current peaks up to -160 A, which equals a current demand of 4 C (see Fig. 26).

Especially at the high current part between 1000 s and 1600 s the increase in temperature for the aged battery cell is significantly higher than for the new battery cell (Fig. 25). The reason for the different temperature gradients can be found in the tracked overall resistance of the battery cells which is also shown in Fig. 26. During high current demand the overall resistance of the battery cell decreases which is an expected behavior because due to the current flow the temperature of the cell increases which again results in a lower resistance [7]. Although the ohmic voltage drop caused by solid conductors inside the battery increases as the temperature increases, the conductivity of the electrolyte for example increases



Fig. 21. State of charge determination based on counting the flowing charge.

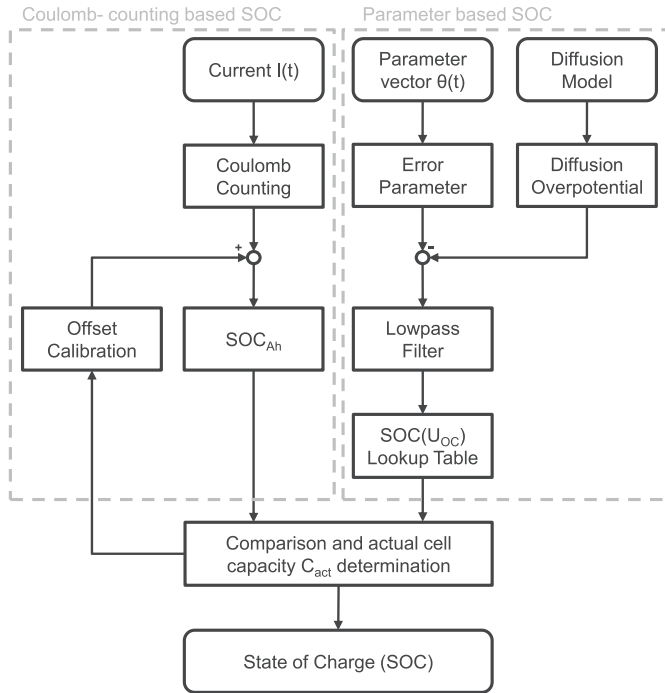


Fig. 22. State of charge determination procedure.

too. The lithium ions which represent the charge inside the electrolyte can move faster. Furthermore, the speed of diffusion inside the solid electrodes increases too [29]. This counteracts the increase in resistances and results in an overall resistance decrease as the temperature increases. Still the average overall resistance increases in dependency of the ageing of the battery cell and the temperature.

12.3. State of health tracking during a long term test

The purpose of the long term state of health tracking test is to evaluate the ability of tracking the overall resistance as a function of aging. It shall be shown that the online tracking of the fast dynamic parameters R_i , R_{ct} and C_{dl} can be used to detect aging processes of the battery cell. A Sanyo (cell S-1) 2 Ah NMC lithium-ion battery is exposed to a series of repeating current cycles over a period of about seven months. Over that period of time the total resistance of the battery cell is measured and recorded. The battery will experience 6236 current cycles shown in Fig. 24. For the evaluation 33 samples at discrete time steps, each containing two current cycles, are taken out of the entire test and fed into the parameter identification algorithm. The identified parameters are recorded and compared to the measured values. The test is conducted at 20 °C.

12.3.1. Results of state of health tracking

The results are presented in 26. The overall absolute resistance is presented as well as the relative increase in resistance. The latter has been calculated according to Eq. (52).

$$R_{rel}(t) = \frac{R_{all}(t)}{R_{all}(1)} \cdot 100\% \quad (52)$$

At the beginning of the test the resistance of the new battery cell is at about 40 mΩ. It increases to values up to 52 mΩ. At about 4.5 months a sudden increase in resistance is noticeable. The reason for this cause is unknown, since analysis of available data does neither lead to a unique reason. However, the parameter identification process can track the increase of the battery cell resistance. Therefore it can be used to monitor the aging process of the battery cell when the algorithm is used in a battery management system. Another interesting aspects is the decrease in the double layer capacitance C_{dl} which is presented in Fig. 27. Beginning at about 3 F it decreases to less than 2.4 F. Again at about 4.5 months a sudden increase is noticeable which cause is most likely related to the

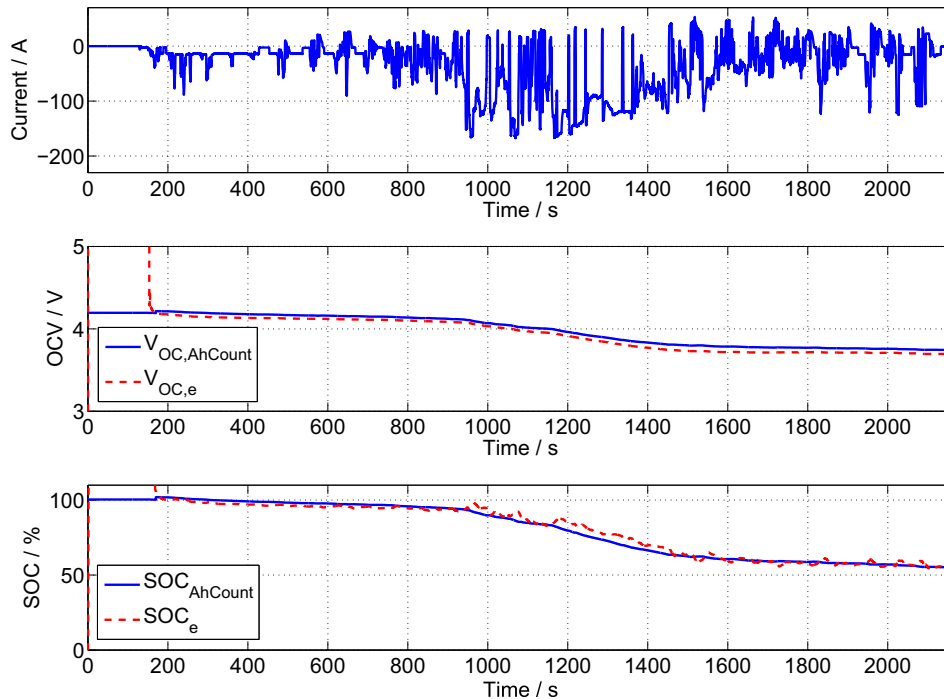


Fig. 23. Comparison of both state of charge filters under high current demand.

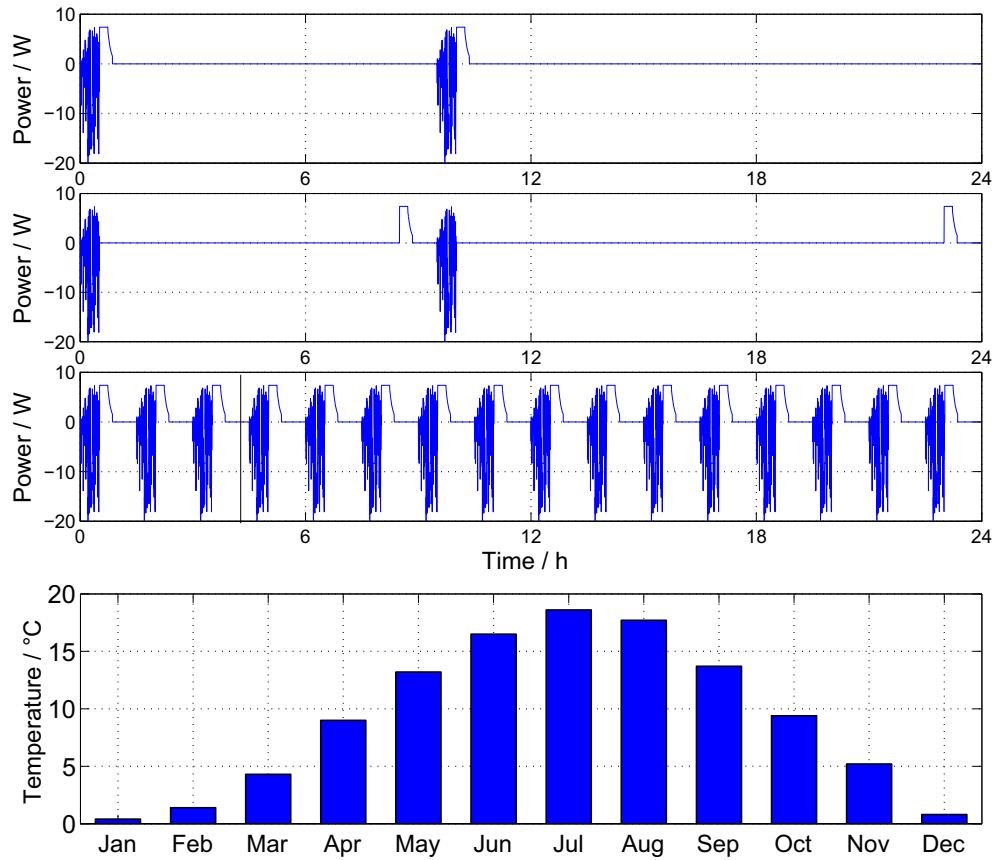


Fig. 24. (top) Three power profiles over time for battery aging; 1) charge after driving, 2) charge before driving and 3) no rest periods; (bottom) Temperatures used for algorithm verification. For each month an ambient temperature is given to the proposed monitoring algorithm. Values are average temperatures for Germany from 2001–2010 [25].

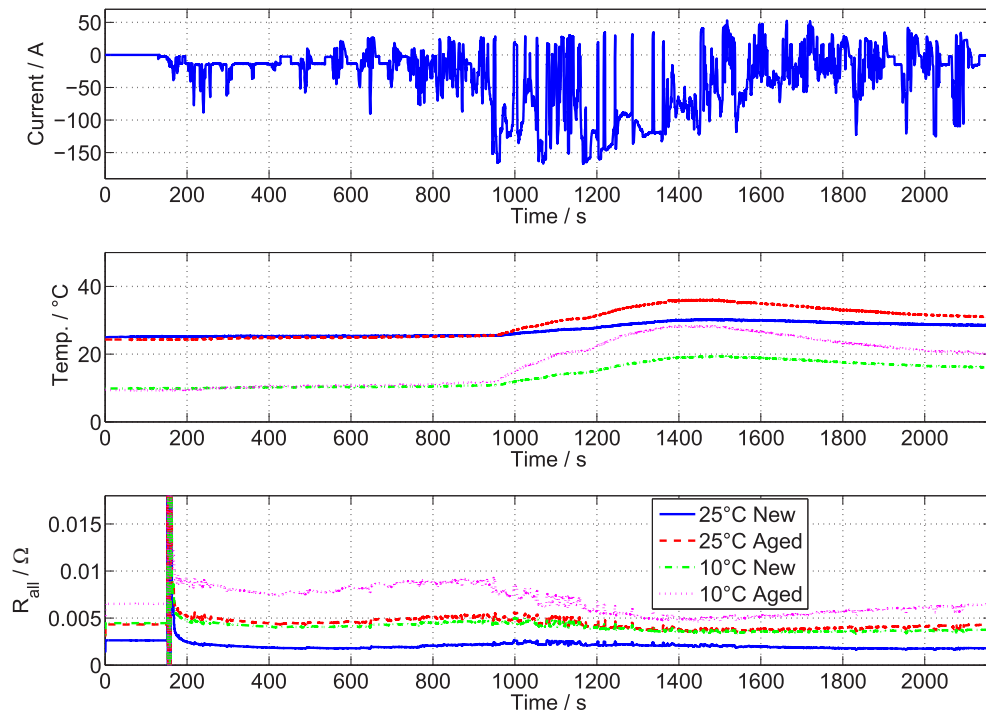


Fig. 25. Temperature change in dependency of age during a high current demand cycle.

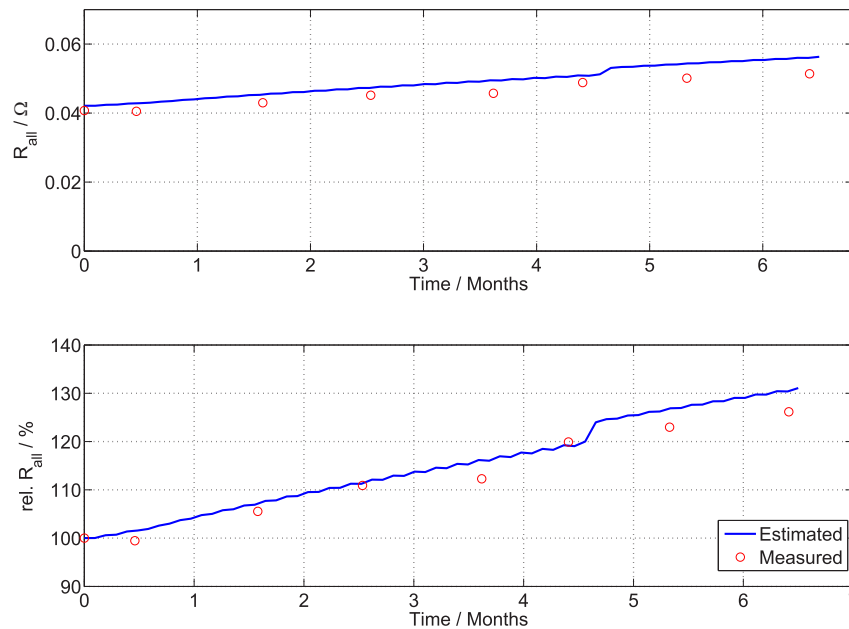


Fig. 26. Overall Resistance during long term aging test.

sudden increase of resistance at the same point in time. Still the decrease in the capability of forming a double-layer capacitance between the electrodes and the electrolyte provides an interesting mean for keeping track of the aging process of the battery. It can be argued that, due to aging, the battery is not capable of providing the same surface at the electrode for the charge-transfer process as before the aging process started. This results in a less developed Helmholtz double layer at the interface between the electrodes and the electrolyte because the surface area reduces as the battery ages. Furthermore, a built-up of the solid electrolyte interface results in a change of relative permittivity ϵ_r . This effect might also cause a change in the double-layer capacitance.

12.4. State of health tracking during a city driving cycle

To verify the relationship among the state of health of a battery, identified resistances and double-layer capacitance another test with a conventional city driving cycle is conducted. Again a new Kokam 40 Ah NMC lithium-ion battery cell with a remaining capacity of 42 Ah and an aged battery cell with 38 Ah remaining capacity is used at two different temperatures. The city driving cycle consists of several accelerate and breaking moments as well as a period of medium speed driving which requires a current of

about 60 A. During acceleration the current demand rises up to 160 A. The results for the temperature and resistance tracking are presented in Figs. 28 and 29. It shows a part of the entire driving cycle of 19 min.

As expected the impedance rises as a function of aging and temperature. Furthermore, it becomes obvious that the risen overall resistance must be responsible for the higher temperature increase of the battery cell during high current demands. The impedance between the new and the aged cell at 25 °C rises from 1.4 mΩ to 3.5 mΩ, which equals an increase of 150%. At a temperature of 10 °C the impedance rises from 2.6 mΩ to 7.1 mΩ, which equals an increase of 173%. This can be seen as an indicator that battery cells ability to work at deep temperatures degrades as a consequence of aging. The course of the double-layer capacitance over aging also reflects the influence of aging on the battery cell. As the battery ages the estimated capacitance of the Helmholtz double-layer decreases. The reason for the impedance increase and the double-layer capacitance decrease must be the aging process of the battery. The build-up of the solid electrolyte interface (SEI) causes an impedance increase. Especially during lower SoC, lithium-ions are consumed during the build-up of the SEI which can explain the decrease in the capability of forming a Helmholtz double-layer at the transition between the electrode and the

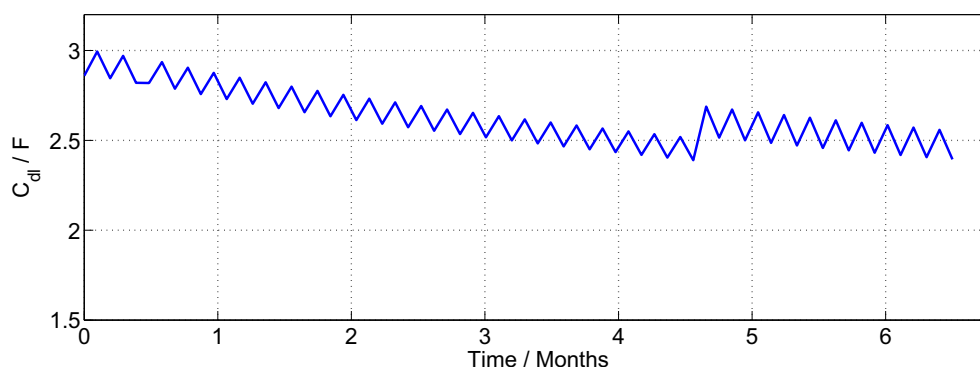


Fig. 27. Decrease in the double layer capacitance during long term aging test.

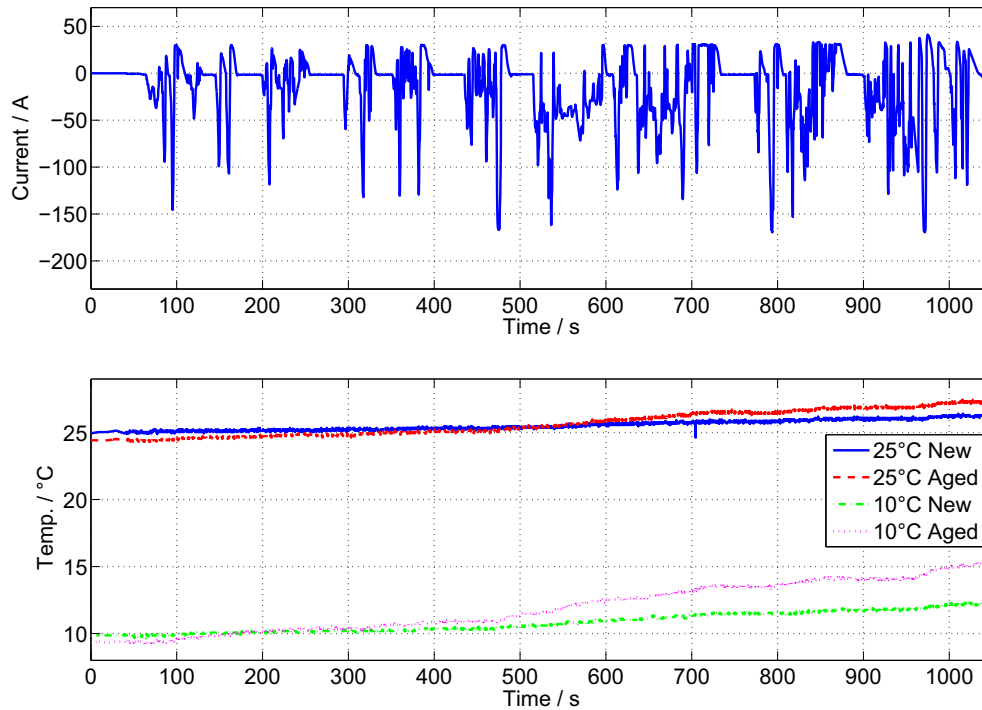


Fig. 28. Tracked parameters during city driving and temperature profile for new and aged Kokam 40 Ah cells.

electrolyte. Further aging processes such as the degradation of conducting salt and reduction of active electrode surface [30] can explain the behavior observed in the experiments. All experiments verify that the parameter tracking algorithm is capable of tracking the state of health by evaluating the increase in overall resistance and decrease in the double-layer capacitance.

The proposed parameter identification and state determination method has been tested for lithium-ion batteries that contain

nickel–manganese–cobalt electrode-material. Novel lithium-ion batteries are based on iron-phosphate cathodes which show hysteresis in the electromotive force between charging- and discharging operation [4]. A promising approach for describing the hysteresis characteristic has been presented by Roscher et al. in Ref. [31]. To ensure adaptability and stability the developed battery monitoring algorithms were applied to a lithium-ion LFP-battery cell O-1 with 8 Ah capacity. The aged battery cell O-2 has a

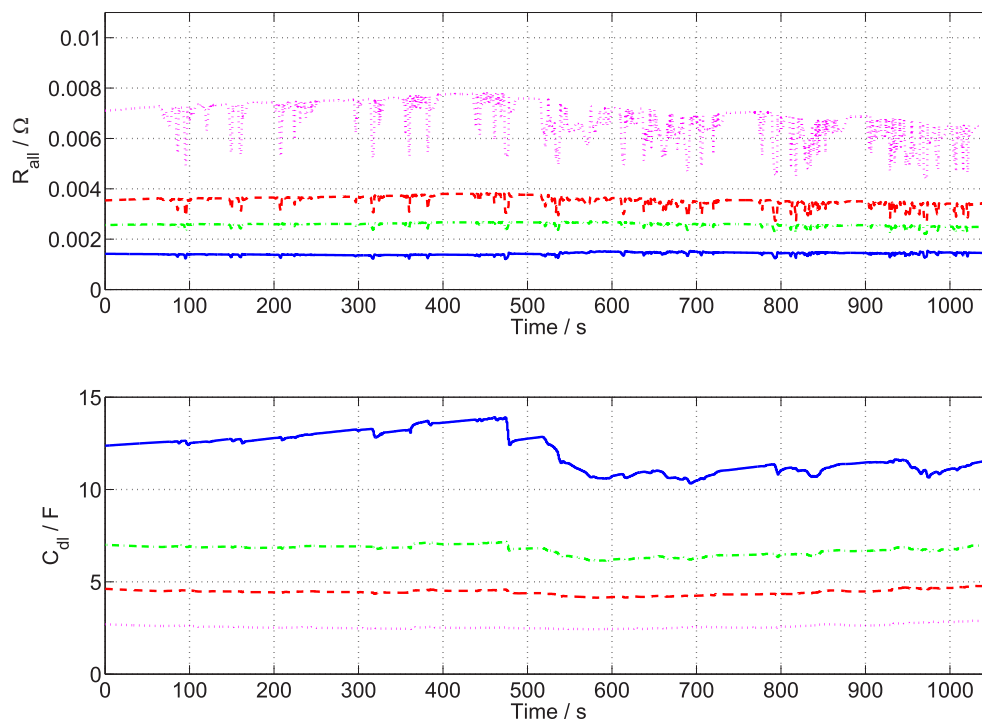


Fig. 29. Tracked parameters R_{all} and C_{dl} during city driving for new and aged Kokam 40 Ah cells.

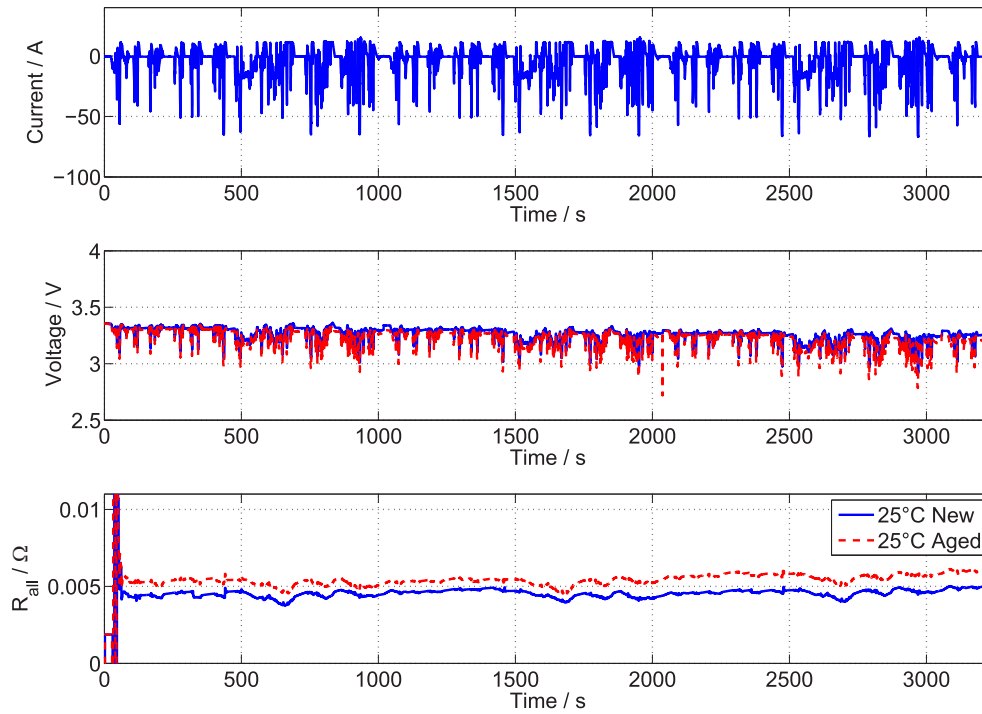


Fig. 30. Tracked overall resistance of an iron-phosphate based lithium-ion 8 Ah cell from o.m.t. GmbH.

remaining capacity of 7.1 Ah and as shown in Figs. 30 and 31, the algorithm is capable to deliver reliable parameters.

13. State of function tracking

A third important state of the battery is the battery's state of function. It serves as an indicator on how well the battery can cope

with upcoming power demands. A battery cell can operate within a specified voltage window. In the case of the Kokam 40 Ah battery cell the specification states a voltage window of 2.7 V up to 4.2 V. During discharge the terminal voltage of the battery drops depending on the current demand. This behavior limits the maximum current that can be drawn from the battery. On the other hand charging operation leads to an increase of terminal voltage. The increase also depends on

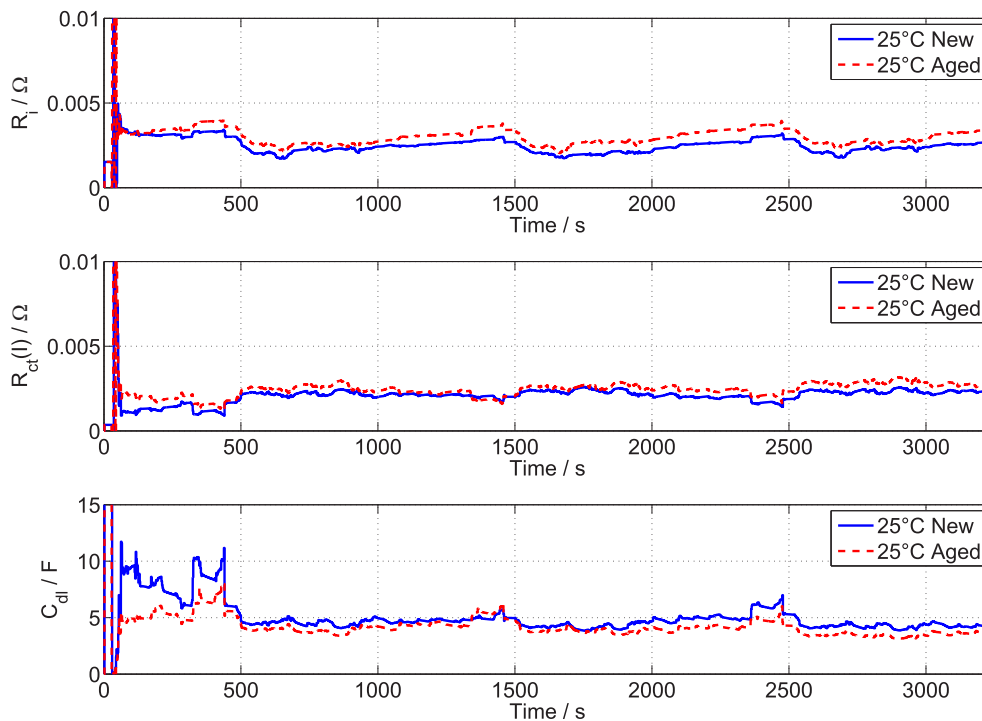


Fig. 31. Tracked R_i , $R_{ct}(I)$ and C_{dl} of an iron-phosphate based lithium-ion 8 Ah cell from o.m.t. GmbH.

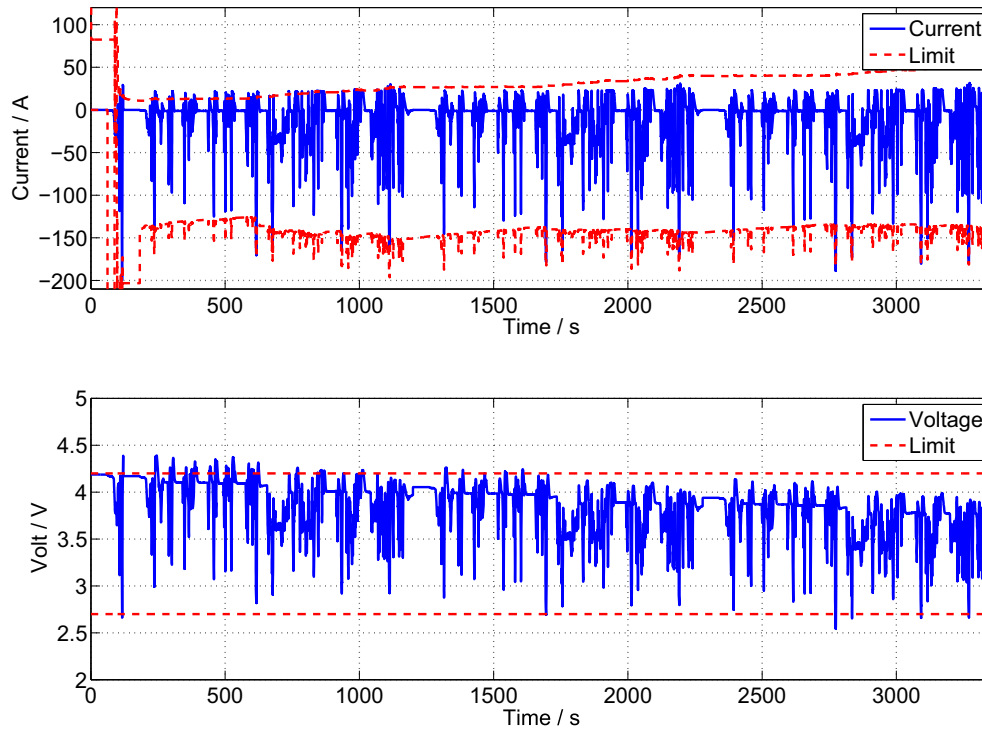


Fig. 32. Current limits as an indicator for the state of function.

the rate of current fed into the battery. This behavior limits the maximum current that can be used to charge the battery. The maximum rate of current that can be fed in or withdrawn from the battery can be used as an indicator for the state of function. Therefore it is necessary to know, which current-rates result in an overpotential that causes a terminal voltage outside the specified voltage window.

The maximal available power depends on the maximal available current. The maximal available current depends on the open-circuit

voltage U_{oc} as a function of the state of charge and the resistance of the battery cell. As mentioned in Section 12.2 the resistance is directly depending on temperature and the battery cells aging status. The parameter identification algorithm provides the resistances of the battery and these parameters can be used to determine the current-rate that does not cause a violation of the voltage-window. The current and power capability of the battery cell can be calculated as given in Eqs. (53) and (54).

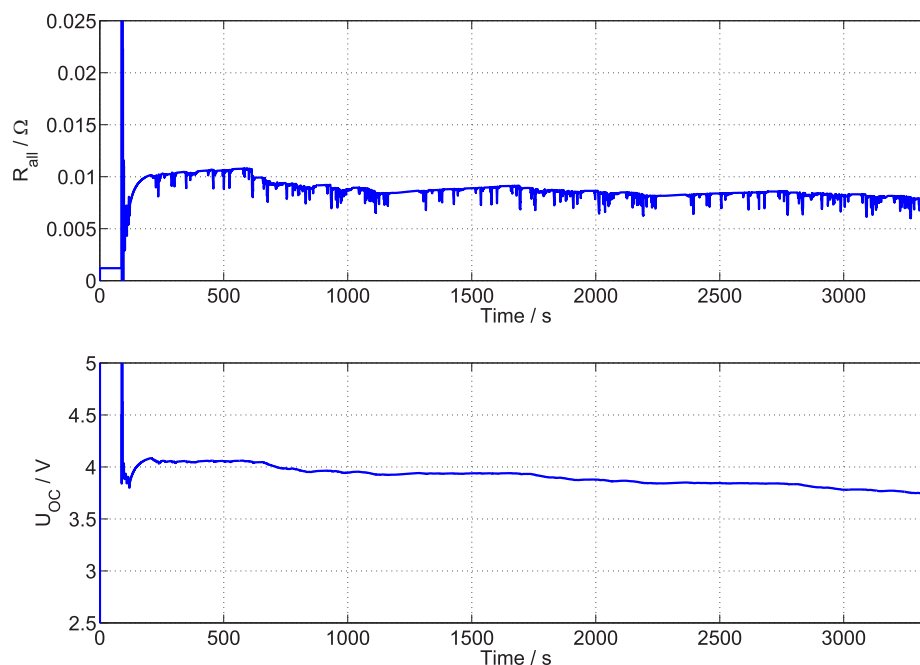


Fig. 33. Overall resistance and open-circuit voltage during current cycles.

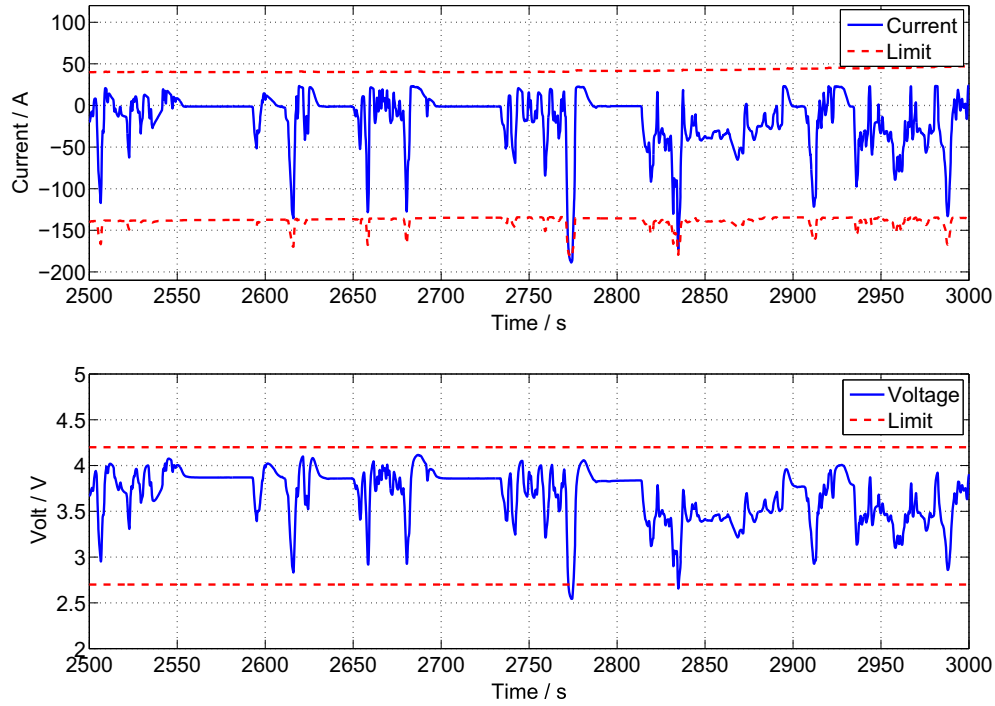


Fig. 34. Current rate limit violation resulting in critical voltage drop.

$$i_{\max} = \frac{U_{\text{limit}} - U_{\text{oc}}}{R_i + R_{\text{ct}} + R_d} \quad (53)$$

$$P_{\text{available}} = U_{\text{limit}} \cdot \frac{U_{\text{limit}} - U_{\text{oc}}}{R_i + R_{\text{ct}} + R_d} \quad (54)$$

The critical voltage U_{limit} depends on the direction of the current. The result of the maximum current rate calculation can be handed over to the battery management system and the energy distribution system of the vehicle to prevent current requests that

would violate battery specifications. Especially aged batteries operating at low temperatures have limited power capability. Fig. 32 shows the maximum current rate that can be withdrawn from the battery cell without causing the battery voltage to go below the critical voltage of 2.7 V or above the maximal voltage of 4.2 V. The battery is a Kokam 40 Ah battery cell which is aged to a remaining capacity of 38 Ah and operated at 0 °C. At 2750 s the maximum discharge current rate is –150 A. However the battery is discharged with –190 A which results in a terminal voltage of 2.55 V. That is below the minimal specified voltage of 2.7 V. Therefore the battery should not have been discharged with such a high current at that moment. If the current is limited to –150 A the battery will not have violated the minimal allowable voltage. The same applies for the maximum charge current which has been violated especially at full state of charge between 100 s and 700 s. Notable is the influence of the Butler–Volmer kinetics on the overall resistance, as can be seen in Fig. 33. At high currents the overall resistance drops due to Eq. (21). The influence of the Butler–Volmer kinetics on the charge-transfer resistance must be considered otherwise several more current limit violations are recorded although the voltage has not had dropped below the critical limit (see Fig. 34).

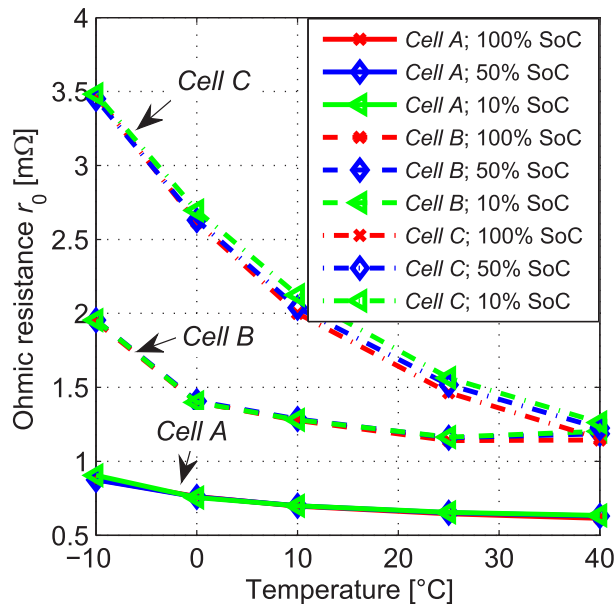


Fig. 35. Pure ohmic resistance and its dependency on the battery temperature and SoC [22].

14. Convergence analysis

Compared to other recursive filters, the RLS shows an extremely fast convergence [32,33] which is considered to be optimal in practice. The convergence is unrelated in regards to the input signal spectrum, while its performance is in favor to eg. LMS algorithm. Choosing the forgetting factor λ as described before, the convergence and adaptation of parameters is slowed (until no adaptation) or accelerated without introducing numerical stability problems in the RLS adaptive filter. As described in Ref. [32] RLS filters are highly stable, the high initial convergence speed is independent of signal Eigenvalue spread, and less steady state error compared to other filters such as LMS, NLMS [33,34]. Furthermore, we introduce a

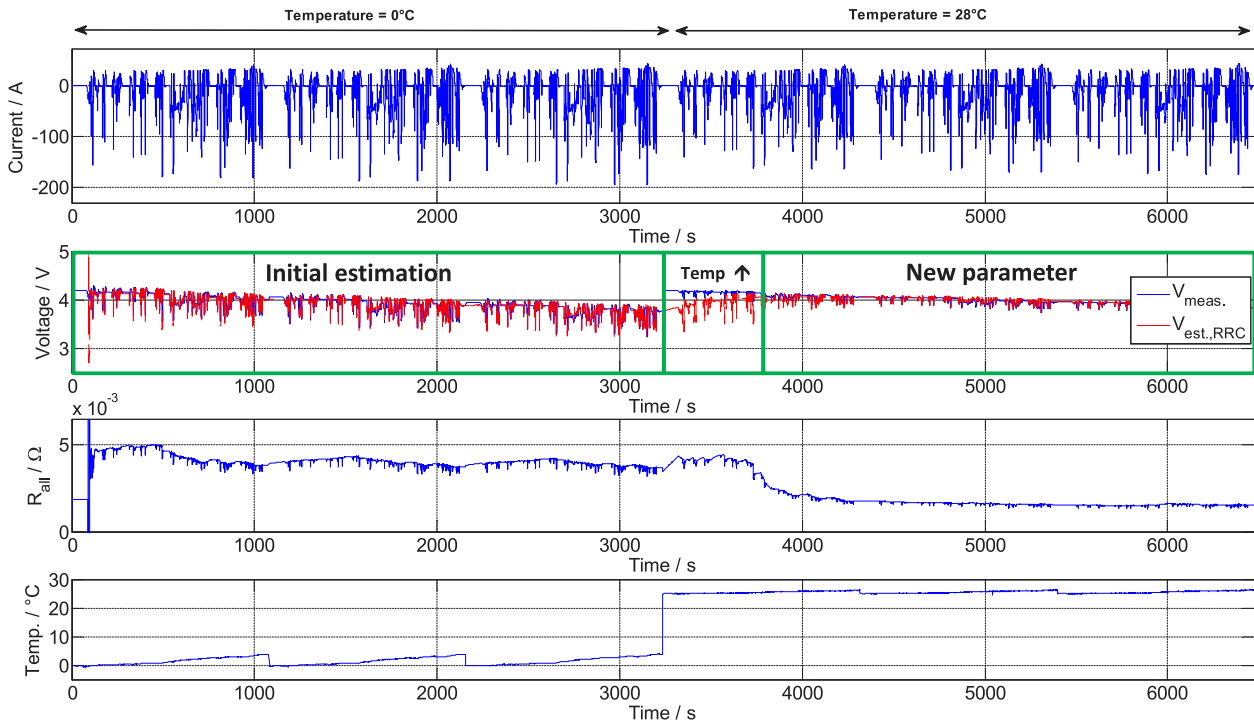


Fig. 36. Prove of convergence for Cell K-A while distinguishing between aging and temperature effects for fast temperature changes.

matrix inverse lemma Eq. (19), here the numerical stability of the estimator must be ensured, therefore, division by zero is checked and low values are neglected for this time step. The following scenario proves that the convergence to correct battery impedance parameters is given due to distinguishing between aging and temperature effects also for fast temperature changes. This is especially difficult since the ohmic resistance is dominated by the

electrolyte, resulting in an increase for decreasing temperature [10]. Fig. 35 illustrates this behavior for the Kokam SLPB100216216H battery with NMC cathode material and different aging states, Cell K-A is new, Cell K-B moderately aged while Cell K-C is in a significantly aged state [22].

The current profile consists of 2 different data sets, starting with a new battery Cell K-A at 0 °C the temperature changes suddenly to

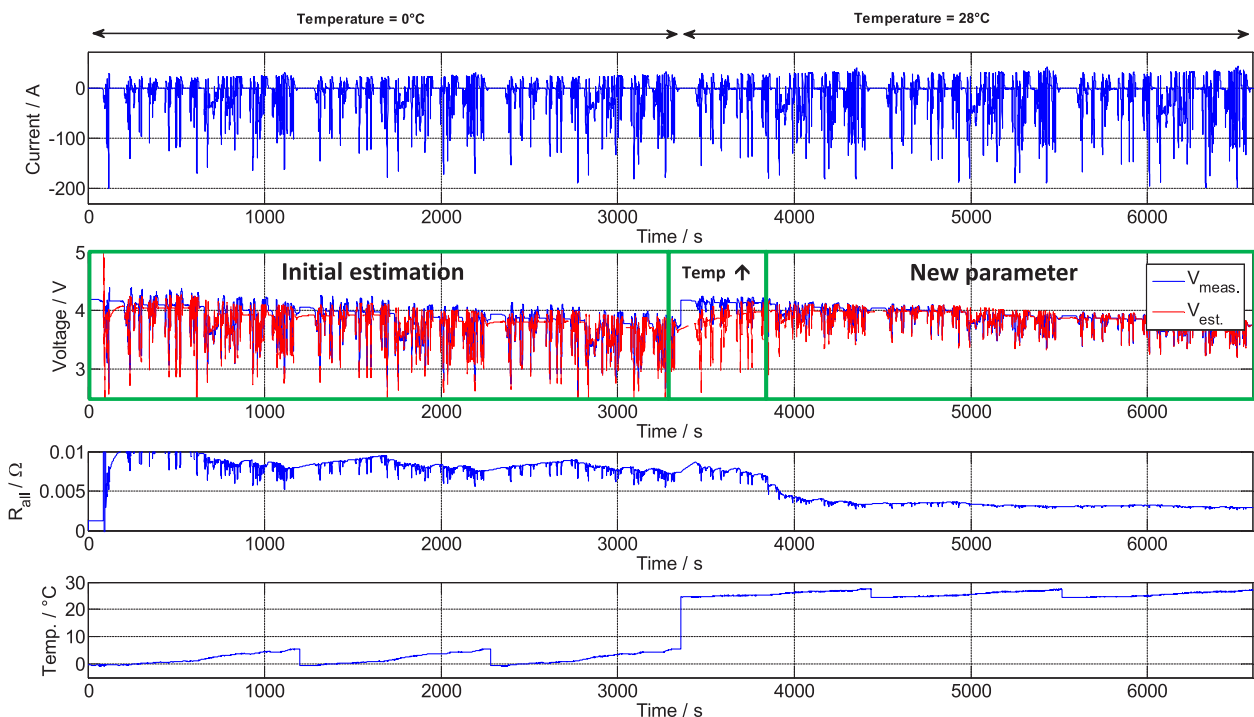


Fig. 37. Prove of convergence for Cell K-C while distinguishing between aging and temperature effects for fast temperature changes.

28 °C at 3200 s. As can be seen in Fig. 36, the algorithm is able to converge to the correct parameters while the voltage error at the temperature transition at 3200 s decreases to a minimum. At the same time, the internal resistance decreases due to temperature increase. The same trend can be observed in Fig. 35, however, the algorithm considers charge transfer and diffusion resistances as well.

The second current profile also consists of 2 different data sets, starting with an aged battery Cell K-C at 0 °C the temperature changes suddenly to 28 °C at 3200 s. Once again the algorithm is able to converge to the correct parameters, presented by voltage error minimization and consistency with the test findings in Fig. 35.

The simulations in Figs. 36 and 37 show, that the algorithm not only converges to correct impedance parameters, but also distinguishes between aging and temperature effects also for fast temperature changes. It is illustrated that a change of R_{all} from Cell K-A to Cell K-C for 0 °C is given by 5 mΩ to 10 mΩ while from Cell K-A to Cell K-C for 28 °C is increased from 1.5 mΩ to 4 mΩ. Both simulations also prove that the internal resistance decreases due to temperature increase.

15. Conclusion

In this series of two papers, we have introduced how sophisticated battery monitoring algorithms based on a memory optimized RWLS estimator might be used in BMS applications.

In this paper we present a novel method to determine the states of a lithium-ion battery. Identification of the parameters of a battery model allows an evaluation of the states of the battery by keeping track of parameter changes.

In the earlier paper a model for the battery system has been presented. A parameter identification technique has been developed. The results of the parameter identification are used to evaluate the states of the battery. The following advances have been made.

1. A least-square based parameter identification algorithm has been developed which allows an efficient online identification of the high dynamic elements of a battery model. The identification algorithm is fully recursive and can easily be implemented on an embedded system.
2. The battery model has been extended by incorporating a current depending charge-transfer resistance. Most battery models employed in BMS, assume linear dependency of the charge-transfer resistance on the current. It has been proven that due to the Butler–Volmer equation a nonlinear characteristic is observable. The influence of the Butler–Volmer kinetics on the charge-transfer process has been identified using a novel mutation based algorithm. The proposed algorithm can run online and in parallel to the introduced least-square parameter estimator and thus is easily implementable on a hardware platform.
3. A Warburg element represents the mass transport effects occurring during operation of the lithium-ion battery. A novel approach to describe a time-domain model of the diffusion process in the state-space has been introduced. Furthermore the parameters of the state-space model are determined by an off-line greybox parameter technique. The incorporation of the diffusion process in the battery model allows a more precise determination of the battery states.
4. A novel state of charge determination algorithm has been developed which bases on the residual term of the least-square parameter identification algorithm. It allows a re-calibration of a conventional coulomb-counting state of charge determination regime during operation making the system suitable for online tracking of the state-of-charge without the need of a reference point of the state of charge.
5. Because the parameters of the battery model are updated online, the state of health can be tracked by observing the change of resistance. Especially the increase of the charge-transfer resistance reflects and the decrease of stiffness in the charge-transfer process reflects the aging process. Furthermore a novel observation of the double-layer capacitance allows an alternative way of determining the state of health.
6. To evaluate the state of function, the power capability of the battery is analyzed by evaluating the identified resistances of the battery model. It has been shown that the power capability prediction allows a very precise definition of the state of function.
7. The proposed battery state determination regime has been successfully tested for lithium-ion batteries that contain nickel–manganese–cobalt electrode-material as well as lithium iron-phosphate with current cycles that represent real driving cycles of an electric vehicle. This underlines the ability of the proposed system to work in the field.
8. A convergence analysis was carried out and simulations show that the algorithm is able to distinguish between aging and temperature effects also for fast temperature changes.

References

- [1] L. Ljung, *System Identification Theory for the User*, second ed., Prentice Hall Inc., Upper Saddle River, 1999.
- [2] V. Pop, H.J. Bergveld, D. Danilov, P. Regtien, P. Notten, *Battery Management Systems Accurate State-of-Charge Indication*, in: Philips Research Book Series, vol. 9, Springer, Netherlands, Dordrecht, 2008.
- [3] S. Buller, M. Thele, R. De Doncker, E. Karden, *IEEE Trans. Ind. Appl.* 41 (3) (2005) 742–747.
- [4] A.E. Anders, *Effect of Current Dynamics on Li-ion Cell Capacity and Impedance* (Ph.D. thesis), University of Wisconsin, Madison, 2010.
- [5] W. Waag, C. Fleischer, D.U. Sauer, *J. Power Sources* 242 (2013) 548–559, <http://dx.doi.org/10.1016/j.jpowsour.2013.05.111>. URL: <http://www.sciencedirect.com/science/article/pii/S0378775313009014>.
- [6] A. Jossen, W. Weydanz, *Moderne Akkumulatoren richtig einsetzen*, Inge Reichardt Verlag, 2006.
- [7] D. Linden, T.B. Reddy, *Handbook of Batteries*, third ed., McGraw-Hill, New York, 2002.
- [8] I.N. Bronstein, K.A. Semendjajew, G. Musiol, H. Mühlig, *Taschenbuch der Mathematik*, vol. 23, Harri Deutsch Verlag, 2008.
- [9] C. Dyer, P. Moseley, Z. Ogumi, D. Rand, B. Scrosati, J. Garche, *Encyclopedia of Electrochemical Power Sources*, Elsevier Science, 2013. URL: <http://books.google.com/books?id=VrC7faORhX0C>.
- [10] V.R. Subramanian, D. Tapriyal, R.E. White, *Electrochem. Solid-State Lett.* 7 (9) (2004) 259–263.
- [11] J. Tafel, *Z. Phys. Chem.* 50 (1905) 641–712.
- [12] B.S. Bhangu, P. Bentley, D.A. Stone, *IEEE Trans. Veh. Technol.* 54 (2005) 783–794.
- [13] H. Pohlheim, *Evolutionäre Algorithmen*, Springer, Berlin, 1999.
- [14] H. Meyr, *Regelungstechnik II*, RWTH Aachen University, 1981.
- [15] S. Buller, *Impedance Based Simulation Models for Energy Storage Devices in Advanced Automotive Power Systems* (Ph.D. thesis), RWTH Aachen University, 2003.
- [16] V.R. Subramanian, V.D. Diwakar, D. Tapriyal, *J. Electrochem. Soc.* 152 (10) (2005) 2002–2008.
- [17] J. Thielen, *Investigation of the Lithium Ion Mobility in Cyclic Model Compounds and their Ion Conducting Properties*, Johannes Gutenberg-Universität Mainz, 2011 (Ph.D. thesis).
- [18] P. Mauracher, E. Karden, *J. Power Sources* 67 (1) (1997) 69–84.
- [19] O. Böhlen, *Impedance-based Battery Monitoring* (Ph.D. thesis), RWTH Aachen University, 2008.
- [20] W. Waag, S. Kbitz, D.U. Sauer, *Measurement* 46 (10) (2013) 4085–4093.
- [21] W. Waag, S. Kbitz, D.U. Sauer, *Appl. Energy* 102 (0) (2013) 885–897, <http://dx.doi.org/10.1016/j.apenergy.2012.09.030>. URL: <http://www.sciencedirect.com/science/article/pii/S030626191200671X>.
- [22] L. Juang, *Online Battery Monitoring for State-of-Charge and Power Capability Prediction* (Ph.D. thesis), University of Wisconsin, Madison, 2010.
- [23] M.A. Roscher, S. Member, O.S. Böhlen, D.U. Sauer, *IEEE Trans. Energy Convers.* 26 (3) (2011) 737–743.
- [24] J. Schmalstieg, S. Käbitz, M. Ecker, D.U. Sauer, *From Accelerated Aging Tests to a Lifetime Prediction Model: Analyzing Lithium-ion Batteries*, EVS27 International Battery, Hybrid and Fuel Cell Electric Vehicle Symposium, Barcelona.
- [25] H. Blanke, O. Böhlen, S. Buller, R. De Doncker, B. Fricke, A. Hammouche, D. Linzen, M. Thele, D. Sauer, *J. Power Sources* 144 (2) (2005) 418–425.

- [27] O. Bohlen, A. Hammouche, D.U. Sauer, Impedanzbasierte zustandsdiagnose für energiespeicher in automobilen, Tech. Rep., 2006
- [28] P. Singh, R. Vinjamuri, X. Wang, D. Reisner, *Electrochim. Acta* 51 (8) (2006) 1673–1679.
- [29] K.A. Smith, C.D. Rahn, C.-Y. Wang, *Energy Convers. Manag.* 48 (9) (2007) 2565–2578.
- [30] F. Herb, Alterungsmechanismen in Lithium-Ionen-Batterien und PEM-Brennstoffzellen und deren Einfluss auf die Eigenschaften von daraus bestehenden Hybrid-Systemen (Ph.D. thesis), Universität Ulm, 2010.
- [31] M.A. Roscher, D.U. Sauer, *J. Power Sources* 196 (1) (2011) 331–336.
- [32] B. Gibbs, *Advanced Kalman Filtering, Least-squares and Modeling: A Practical Handbook*, Wiley, 2011. URL: <http://books.google.com/books?id=VrC7faORhX0C>.
- [33] M. Stridh, *Lecture Notes on ETTN05 Adaptive Signal Processing*, Lund University, Electrical and Information Technology, 2011. URL: <http://www.eit.lth.se/fileadmin/eit/courses/ettn05/notes5.pdf>.
- [34] K.G.J. Dhiman, S. Ahmad, *Int. J. Sci. Eng. Technol. Res.* (2011).